



Sulfur, sulfides, oxides and organic matter aggregated in submarine hydrothermal plumes at 9°50'N East Pacific Rise

J.A. Breier^{a,*}, B.M. Toner^b, S.C. Fakra^c, M.A. Marcus^c, S.N. White^a,
A.M. Thurnherr^d, C.R. German^a

^a Woods Hole Oceanographic Institution, Woods Hole, MA 02543, USA

^b University of Minnesota – Twin Cities, St. Paul, MN 55108, USA

^c Lawrence Berkeley National Lab, Berkeley, CA 94720, USA

^d Lamont-Doherty Earth Observatory, Palisades, NY 10964, USA

Received 1 September 2011; accepted in revised form 3 April 2012; available online 20 April 2012

Abstract

Deep-sea hydrothermal plume particles are known to sequester seawater trace elements and influence ocean-scale biogeochemical budgets. The relative importance of biotic versus abiotic oxidation-reduction and other particle-forming reaction, however, and the mechanisms of seawater trace element sequestration remain unknown. Suspended particulate material was collected from a non-buoyant hydrothermal plume by *in situ* filtration at 9°50'N East Pacific Rise during a 3-day, 24 sample, time-series. Twenty-three samples were digested for total elemental analysis. One representative sample was selected for particle-by-particle geochemical analyses including elemental composition by X-ray fluorescence, speciation of Fe, S, and C by 1s X-ray absorption near edge structure spectroscopy, and X-ray diffraction. Consistent with past studies, positive linear correlations were observed for P, V, As, and Cr with Fe in the bulk chemistry. Arsenic was associated with both Fe oxyhydroxides and sulfides but not uniformly distributed among either mineral type. Particle aggregation was common. Aggregates were composed of minerals embedded in an organic matrix; the minerals ranged from <20 nm to >10 µm in diameter. The speciation of major mineral forming elements (Fe, Mn, S) was complex. Over 20 different minerals were observed, nine of which were either unpredicted by thermodynamic modeling or had no close match in the thermodynamic database. Sulfur-bearing phases consisted of polysulfides (S₆, S₈), and metal sulfides (Fe, Cu, Zn, Mn). Four dominant species, Fe oxyhydroxide, Fe monosulfide, pyrrhotite, and pyrite, accounted for >80% of the Fe present. Particulate Mn was prevalent in both oxidized and reduced minerals. The organic matrix was: (1) always associated with minerals, (2) composed of biomolecules, and (3) rich in S. Possible sources of this S-rich organic matter include entrained near vent biomass and *in situ* production by S-oxidizing microorganisms. These results indicate that particle aggregation with organic material is prevalent in dispersing hydrothermal plume fluxes, as well as in sinking particulate matter at this site. Particle aggregation and organic coatings can influence the reactivity, transport, and residence time of hydrothermal particles in the water column. Thus a biogeochemical approach is critical to understanding the net effect of hydrothermal fluxes on ocean and sedimentary trace element budgets.

© 2012 Elsevier Ltd. All rights reserved.

1. INTRODUCTION

Previous hydrothermal studies have developed a conceptual model of the inorganic processes associated with

hydrothermal plume formation (Rudnicki and Elderfield, 1993; Elderfield and Schultz, 1996), and estimates of their associated chemical fluxes (Kadko, 1993). That conceptual model considers two inorganic (and abiotic) processes. *Process I* occurs immediately upon discharge of vent fluid into the ocean: Fe(II) and other chalcophile elements co-precipitate to form polymetallic sulfide phases. *Process II* occurs as reduced vent-fluids rise and mix with more oxidizing

* Corresponding author. Tel.: +1 508 289 2932; fax: +1 508 457 2191.

E-mail address: jbreier@whoi.edu (J.A. Breier).

ambient seawater to precipitate Fe oxyhydroxides. *Process I* results in the accumulation of seafloor metal sulfide rich sediment deposits near vent sites and removes a large fraction of vent fluid Fe (Rudnicki and Elderfield, 1993; Kadko et al., 1995; Field and Sherrell, 2000), though the extent of this removal remains uncertain (Bennett et al., 2008; Yucel et al., 2011). *Process II* generates finer particles rich in Fe(III)-bearing minerals and is considered the primary mechanism for hydrothermal scavenging of seawater trace elements (Trocine and Trefry, 1988; Feely et al., 1990, 1991; German et al., 1990, 1991a,b; Kadko et al., 1994). Neither organic geochemical nor microbial processes were considered in these earlier studies.

Evidence for both microbial processes and organic-rich material within hydrothermal plumes has, however, been building for decades. Winn et al. (1986) and Cowen et al. (1986) measured elevated microbial biomass and cell concentrations in the hydrothermal plumes of the Juan de Fuca Ridge. O'Brien et al. (1998) reported the presence of elevated microbial biomass, particularly archaea, among hydrothermal plume particles at the Rainbow hydrothermal field, Mid-Atlantic Ridge. Biomass, biomolecules (transparent exopolymers, ascending/descending lipids), and mineral aggregates coated with an organic matrix have since been observed within hydrothermal plumes (Cowen et al., 2001; Wakeham et al., 2001; Shackelford and Cowen, 2006; Toner et al., 2009). Microbial CH₄, NH₄⁺, and Mn oxidation within nonbuoyant plumes has been reported (De Angelis et al., 1993; Mandernack and Tebo, 1993; O'Brien et al., 1998; Lam et al., 2008), and the presence of Mn oxidizing microbial communities within plumes at Guaymas Basin is now established (Dick et al., 2009). Estimates of chemical energy available in plumes suggest other metabolic pathways are also possible (McCollom, 2000). Seafloor hydrothermal “snow-blower” vents demonstrate that microbial activity fueled by H₂S oxidation can influence the composition of particles in near-bottom water, rising plumes, and perhaps nonbuoyant plumes during episodes of volcanic seafloor eruption (Haymon et al., 1993; Feely et al., 1994; Taylor and Wirsen, 1997).

Insights from recent studies show that models for hydrothermal plumes must account for interactions between organic molecules and metals such as Fe and Cu (Sander and Koschinsky, 2011). Both dissolved and particulate organic C can stabilize metals in plumes against precipitation as poorly soluble minerals (Sander et al., 2007; Bennett et al., 2008; Toner et al., 2009). Complexes with organic ligands were observed to stabilize approximately 4% of Fe as dissolved Fe(III) in nonbuoyant plumes near 5°S Mid-Atlantic Ridge (Bennett et al., 2008). Particulate organic C enriched in Fe(II) was observed in sinking hydrothermal plume material at 9°50'N East Pacific Rise (EPR) (Toner et al., 2009). Particulate organic C has also recently been shown to be enriched in rising and non-buoyant plume suspended material at 9°50'N East Pacific Rise (Bennett et al., 2011). These insights are leading to reconsideration of hydrothermal flux estimates. In the case of the Fe cycle, recent estimates indicate that hydrothermal plumes may supply up to 25% of all deep-ocean dissolved Fe (Bennett et al., 2008), and buffer the ocean Fe cycle, over time-scales

of ka, against shorter-term processes such as aerosol deposition (Tagliabue et al., 2010).

Mineral precipitation, surface reactivity, and particle morphology can (i) influence the transport and fate of hydrothermal material and (ii) be altered by microbial oxidation/reduction, metal complexation, particle coatings, and aggregation processes. An accurate understanding of how these processes modify the hydrothermal exchange of material between the seafloor and the oceans requires a biogeochemical and mechanistic approach to plume modeling. To this end, we have recently developed a new sampling tool, the Suspended Particulate Rosette (SUPR) sampler that can collect multiple discrete particle samples (up to 24 per deployment) from different locations within rising and laterally spreading hydrothermal plumes (Breier et al., 2009). Here, we report the results obtained from the first 3-day time-series of particulate samples that were collected using this SUPR sampler. This deployment was on a short seafloor mooring, at nonbuoyant plume height within the “Hole to Hell” area of 9°50'N on the EPR, within <250 m of high temperature venting. Twenty-three samples were analyzed for bulk particulate Fe, Mn, Al, Cu, Cr, P, V, As, Ba, and light rare earth element (LREE) concentrations. One representative sample was selected for particle-by-particle geochemical analysis. For individual particles and aggregates, elemental composition by micro-focused X-ray fluorescence (μ XRF), speciation of Fe, S, and C by 1s X-ray absorption near edge structure (XANES) spectroscopy, and mineralogy by micro X-ray diffraction (μ XRD) were measured using synchrotron radiation X-ray microprobe and scanning transmission X-ray microscopy (STXM). Minerals observed were compared against minerals predicted from thermodynamic equilibrium reaction path modeling. Calculations were made for particle settling velocity and plume geochemistry.

The results presented here reveal morphological and compositional complexity in particles formed in hydrothermal plumes. They show that trace element incorporation by individual mineral particles is nonuniform despite positive linear correlations in the bulk composition. Our results also add to observations of S-rich organic C at the EPR, and suggest a persistent or frequently reoccurring, potentially biotic, supply of this material to the water column. They also confirm that the organic/inorganic micro-aggregates and Fe(II) enriched organic material observed by Toner et al. (2009, 2012) in the sediment trap samples collected from this same area are also present in the overlying water-column plume and not a consequence of post-depositional processes within the sediment trap.

2. SAMPLING AND METHODS

2.1. Study area

Sampling was carried out at the 9° 50' N EPR vent field, during R/V *Atlantis* cruise AT15-26, part of the LADDER study led by L. Mullineaux (Fig. 1a and b). The SUPR sampler (Breier et al., 2009) was positioned on-axis in the middle of the “Hole to Hell” area centered within the lava flow formed by the 2005/2006 eruption. The Tica diffuse flow

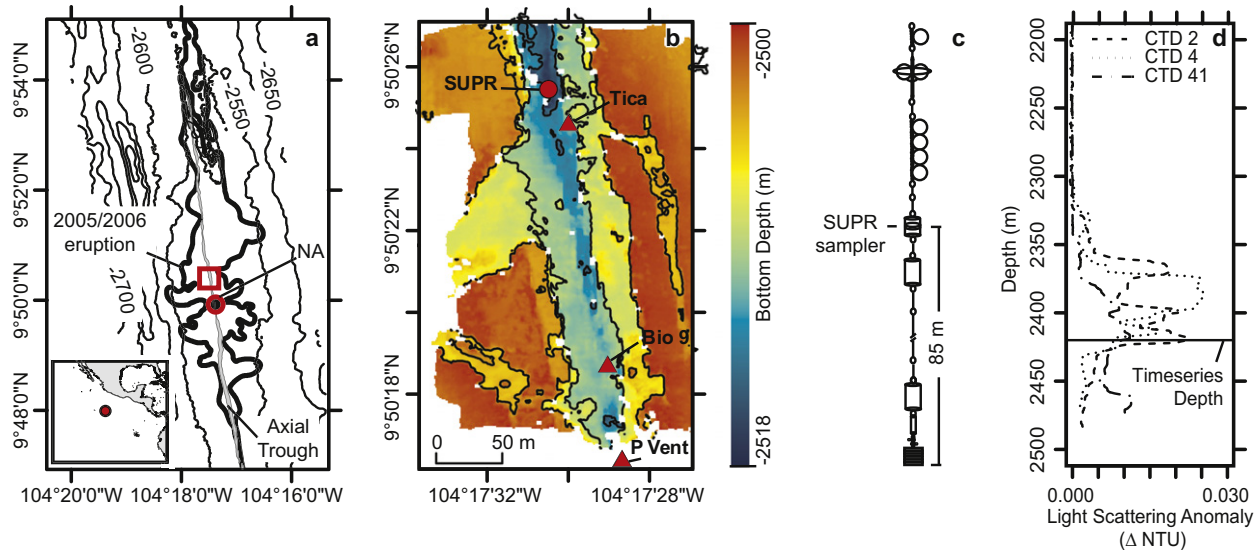


Fig. 1. (a) Location of EPR 9°50'N hydrothermal field and the current mooring designated NA; (b) location of SUPR sampling station within <250 m of the high temperature Bio 9 and P vents; (c) schematic of the mooring used to deploy the SUPR sampler 85 m above the seafloor and, hence (d), at nonbuoyant plume height as identified by optical backscatter profiles. Regional scale bathymetry in (a) is from White et al. (2006), the interpretation of the axial trough and 2005/2006 eruption lava flow are from Soule et al. (2007), and the high (25 cm) resolution bathymetry of the Tica area is from Ferrini et al. (2007). Bathymetric contours are 50 m in (a) and 1 m in (b).

area and high temperature “black smokers”, Bio9 vent and P vent, are within this area (Carbotte and MacDonald, 1992; Shank et al., 1998; Ferrini et al., 2007; Soule et al., 2007). This portion of the EPR is volcanically active and seafloor morphology, venting, and vent fluid chemistry have changed significantly over the past two decades (Haymon et al., 1993; Fornari et al., 1998; Von Damm, 2004; Tolstoy et al., 2006).

2.2. Sample collection and handling

Particulate samples were collected with the Suspended Particulate Rosette (SUPR) sampler positioned 85 m above bottom (bottom depth of 2511 m) at non-buoyant plume height, on a mooring designed for larval sampling (Fig. 1c). Vertical plume structure was identified from multiple nearby CTD profiles, made before and after the mooring deployment, using optical backscatter as measured by a Seapoint turbidity sensor (Fig. 1d). Water velocities at the same depth were recorded every 20 min by an Aanderaa RCM11 current meter on LADDER mooring NA, which was located <1 km south (Fig. 1a) (Thurnherr et al., 2011).

All pre- and post-deployment filter handling was performed within a shipboard fabricated polyethylene enclosure. The SUPR sampler was loaded with acid cleaned (in 10% Seastar HCl), distilled/deionized water rinsed, 37 mm diameter polycarbonate (GE Osmonics) filters; 1 µm filters were used for all sample positions except 3, 12, and 20, which were loaded with 0.2 µm filters. All samples were rinsed upon recovery with distilled/deionized water to remove sea salts and immediately frozen until analysis. The sampler was programmed to: (a) collect 24 evenly distributed time-series samples with the first starting at 0600 on 23 Nov. 2007 and the last starting at 0600 on 26 Nov. 2007;

and (b) maximize the filtered water volume for each sample. In order to prevent filter rupture, the control system varies pumping rate based on feedback from the pumping system between an initial maximum of 7 L min⁻¹ down to 4 L min⁻¹ and stops sample collection once the lower flow rate threshold is reached or if there is an indication of filter rupture, i.e., a sudden increase in pump revolutions per minute. Thus, the filtered volumes and the collection times varied by sample within the ranges of 2–100 L and 30 s to 30 min. For sample 17 pumping was aborted due to an indication of filter rupture; and, for samples 3, 12, and 20 the smaller pore size reduced the flow-rate below the minimum threshold almost immediately. Virtually no material was collected from these four samples and, consequently no results for these samples are presented.

Individual filter volumes are based on a laboratory calibration of the pumping system's digital revolution counter and mechanical flow meter. For autonomous deployments, the digital volume measurements are compared with the total filtered volume per deployment as recorded by the mechanical flow meter and the individual digital volume estimates are then adjusted by distributing the difference proportionally. We estimate that the uncertainty of these adjusted sample volumes is <10% of the actual volumes pumped for values in the range 10–100 L, but that this uncertainty increases for sample volumes less than 10 L. Due to these differences in uncertainties, data presentation and discussion are split between <10 and >10 L samples throughout the remainder of this article.

2.3. Bulk elemental measurements

Filter sample 22, the most visibly loaded sample, was reserved intact for X-ray microprobe and STXM

measurements. The remaining filter samples were all subjected to microwave (Mars 5, General Electric) digestion for 30 min at 220 °C in acid cleaned Teflon vessels using a 10 mL mixture of 50% HNO₃ and 0.01% HF (both Baseline ultrapure grade). This process resulted in the complete digestion of visible particles and in most cases the entire filter. In a few cases small amounts of residual filter material (<1% of the whole filter) remained; this residual was subsequently removed by filtration of the digest solution. A suite of six unused filters, six acid blank solutions, and three portions of the basalt geostandard BHVO-1 (Govindaraju, 1994) were also processed by the same method.

Aliquots of sample digest, at a 1:10 dilution, were analyzed for 22 elements (Tables 1 and 2) by inductively coupled plasma mass spectrometry on a Thermo-Finnigan Element2. Fe, Mn, Al, Cu, Cr, P, V, As, Ba, and LREE concentrations were quantified using external calibration standards. Scandium was added as an internal standard and used to normalize all counts to correct for instrument drift. A desolvating nebulizer (Aridus II, CETAC Technologies) was used for sample introduction to minimize oxide formation and the consequent interferences of Ba, and LREE oxides on Eu and Gd concentrations. To further minimize oxide interferences, ¹⁵³Eu and ¹⁶⁰Gd were used for quantification, thus limiting interferences to ¹³⁷Ba¹⁶O (11% of Ba isotopic composition), ¹⁴⁴Nd¹⁶O (24% of Nd isotopic composition), and ¹⁴⁴Sm¹⁶O (3% of Sm isotopic composition); no corrections were made for these interferences. Precision was determined from three replicate measurements made on each of samples 2, 13, and 23, which were within <5% for the REEs; between 3% and 8% for

Fe, Mn, Al, Cu, Cr, V, As, and Ba; and 12% for P (see Tables 1 and 2). The sample digestion process was monitored using the BHVO-1 geostandard. Elemental recoveries from this basalt standard were >85%, thus recoveries of the more readily soluble material (primarily sulfide, oxyhydroxides, and organic matter) in our samples were assumed to be significantly greater and closer to 100%.

2.4. X-ray microprobe and scanning transmission X-ray microscopy

A polycarbonate membrane filter (sample 22) was divided into four equal quadrants: three quadrants were used in this study. The first analyzed quadrant was used for X-ray microprobe measurements, including: particle-by-particle μXRD, μXRF elemental mapping, Fe 1s and S 1s XANES spectroscopy. Two other quadrants were used for STXM measurements at C 1s and Fe 2p edges: (Prep A) the particles from one of these segments were resuspended in 1 mL of MilliQ, deposited as a droplet (~1 μL) on a silicon nitride membrane (Silson Ltd.), and air-dried; and (Prep B) the particles from the other quadrant were resuspended and rinsed in 1 mL of MilliQ water prior to deposition on a silicon nitride membrane. Because preparation method (A) was sufficient to yield a sample suitable for STXM with no salt crystals present, the sample prepared by method (B) was not used. Concentrating a quarter of the particles from ~100 L of plume water into 1 mL of suspension from which 1 μL is used, allows us to examine particles from an averaged volume of plume water (~25 mL) on one STXM sample window.

Table 1
9°50'N EPR non-buoyant plume particle time series: major and trace elements.

ID	Collection 23-Nov-07	Vol. (L)	Al/ (Al + Fe + Mn)	Al (nM)	Fe (nM)	Mn (nM)	Cu (nM)	Cr (nM)	P (nM)	V (pM)	As (pM)
1	06:00	5	0.96	222 ^a	7.80	0.58	0.41	2.60	1.92	12.9	11.4
2	09:07	90	0.34	0.49	0.85	0.13	0.02	0.02	0.04	1.66	0.69
4	15:23	24	0.41	1.54	1.94	0.29	0.05	0.12	0.11	3.82	1.50
5	18:31	43	0.45	1.03	1.10	0.18	0.02	0.15	0.05	2.73	0.98
6	21:39	19	0.34	0.51	0.84	0.15	0.02	0.12	0.01	2.15	0.82
7	00:46	5	0.25	0.74	2.00	0.19	0.12	0.50	0.00	3.18	1.40
8	03:54	2	0.48	12.2	13.0	0.45	0.09	0.32	0.30	10.4	2.21
9	07:02	7	0.20	0.50	1.78	0.25	0.31	0.23	0.09	3.39	1.33
10	10:10	2	0.30	3.12	6.48	0.67	0.13	1.73	2.69	10.5	4.02
11	13:18	23	0.32	1.59	2.90	0.44	0.02	0.12	0.19	6.16	2.69
13	19:33	64	0.30	0.43	0.90	0.11	0.02	0.01	0.04	1.84	0.90
14	22:41	56	0.40	0.92	1.20	0.17	0.01	0.06	0.10	2.62	1.26
15	01:49	3	0.05	0.16	2.63	0.27	0.09	0.39	0.17	4.53	2.23
16	04:57	3	n.d. ^b	0.00	0.47	0.06	0.00	0.24	0.00	1.90	0.36
18	11:12	3	0.09	0.36	3.30	0.28	0.09	1.15	0.16	7.04	3.29
19	14:20	4	n.d.	0.00	1.59	0.12	0.01	0.25	0.18	2.88	2.96
21	20:36	55	0.31	0.42	0.84	0.11	0.01	0.02	0.05	1.79	0.83
22	23:44	97	Sample analyzed by STXM ^c								
23	02:51	44	0.25	0.29	0.76	0.09	0.01	0.01	0.05	1.65	0.83
24	06:00	12	0.28	1.39	3.28	0.32	0.04	0.28	0.22	6.85	3.71
	26-Nov-07		Precision:	3%	7%	7%	8%	7%	12%	6%	8%

^a Anonymously high Al suggests possibly contamination.

^b Not detectable above background.

^c At the Advanced Light Source, Lawrence Berkeley National Laboratory, Berkeley, California.

Table 2

9°50'N EPR plume particulate time series: barium and light rare earth elements^a.

ID	Collection 23-Nov-07	Vol. (L)	Ba (pM)	La (pM)	Ce (pM)	Pr (pM)	Nd (pM)	Sm (pM)	Eu (pM)	Gd (pM)
1	06:00	5	138	0.442	0.791	0.116	0.435	0.114	0.046	0.104
2	09:07	90	17.7	0.092	0.118	0.022	0.074	0.021	0.005	0.020
4	15:23	24	47.7	0.241	0.328	0.054	0.192	0.053	0.014	0.052
5	18:31	43	33.6	0.133	0.192	0.031	0.112	0.030	0.008	0.029
6	21:39	19	27.7	0.099	0.113	0.022	0.077	0.023	0.005	0.022
7	00:46	5	53.3	n.d. ^b	n.d.	n.d.	n.d.	0.020	0.006	0.021
8	03:54	2	84.1	4.536	5.465	0.549	1.878	0.071	0.179	0.078
9	07:02	7	52.1	0.782	0.824	0.100	0.331	0.033	0.008	0.035
10	10:10	2	164	0.893	1.041	0.181	0.572	0.113	0.038	0.138
11	13:18	23	56.7	0.298	0.309	0.068	0.229	0.069	0.019	0.067
13	19:33	64	16.9	0.085	0.091	0.021	0.068	0.021	0.005	0.020
14	22:41	56	24.0	0.144	0.188	0.033	0.111	0.029	0.076	0.027
15	01:49	3	42.9	0.030	0.000	0.013	0.025	0.032	0.008	0.038
16	04:57	3	16.6	n.d.	n.d.	n.d.	n.d.	n.d.	n.d.	n.d.
18	11:12	3	50.8	0.070	0.000	0.018	0.041	0.037	0.013	0.044
19	14:20	4	20.2	0.502	0.468	0.046	0.184	0.025	0.005	0.027
21	20:36	55	13.5	0.072	0.062	0.017	0.052	0.018	0.005	0.017
22	23:44	97	Sample analyzed by STXM ^c							
23	02:51	44	14.3	0.059	0.062	0.014	0.049	0.016	0.005	0.016
24	06:00	12	49.1	0.318	0.307	0.063	0.213	0.058	0.016	0.057
26-Nov-07										
Average N.W Pacific dissolved LREEs ^d				37.8	4.16	4.84	22.6	4.28	1.17	6.57

^a Precision was 8% for Ba and <5% for the LREEs.^b Not detectable above background.^c At the Advanced Light Source, Lawrence Berkeley National Laboratory, Berkeley, California.^d Alibo and Nozaki (1999); average of dissolved measurements from 1200 to 2600 m.

The mineralogy and S and Fe speciation in the plume particle aggregates (see Tables 3, S1 and S2 in the Appendix A) were characterized using μXRF mapping, S 1s and Fe 1s μXANES, and μXRD at beamline 10.3.2 of the Advanced Light Source (ALS) at Lawrence Berkeley National Laboratory, Berkeley, CA (Marcus et al., 2004). Aggregates were analyzed directly on one quadrant of the original SUPR-deployed polycarbonate membrane filters under ambient conditions. Three randomly chosen areas of the sample, representing 5.384 mm² of the polycarbonate filter, were mapped by μXRF using a Canberra 7-element Ge solid-state fluorescence detector. XRF maps and point spectra were recorded at multiple incident photon energies with a beam spot size of ~5 × 5 μm². Maps were deadtime corrected, registered, and combined into a single composite map that was used to locate aggregates for XANES and XRD analyses. Spectra were calibrated using the inflection point of elemental S at 2472 eV and of Fe foil at 7110.75 eV (Kraft et al., 1996).

Principal component analysis (PCA) and target transformation analysis (TTA) were performed on an Fe XANES dataset (26 spectra; 7010–7410 eV range) to determine the number of species present and evaluate the suitability of standards, using SixPack software (Webb, 2005) and previously described methods (Malinowski, 1977, 1978; Manceau et al., 2002; Toner et al., 2006). Least-squares linear combination fitting (LCF) of experimental spectra was accomplished by ranking combinations of reference spectra (Marcus et al., 2008) using a normalized sum square parameter. The error on the percentages of

species present is estimated to be ±10%. Sulfur XANES data (2420–2575 eV range) were compared to reference spectra. XRD patterns were collected on XANES locations at an incident energy of 17 keV ($\lambda = 0.729 \text{ \AA}$), with 240 s exposure, in transmission mode with a Bruker SMART6K CCD. XRD patterns were radially integrated to obtain profiles as intensity versus 2θ . Calibrations were performed using an Al_2O_3 (alumina) standard, all XRD data were processed with Fit2D (Hammersley et al., 1996) and peak identification was accomplished using JADE software (Materials Data Inc.).

Particle morphology, C and Fe speciation were characterized by STXM at ALS beamline 11.0.2 (Kilcoyne et al., 2003). This microscope employs a Fresnel zone plate lens (25 nm outer zones) to focus a monochromatic X-ray beam onto a scanned sample to record transmission images using a scintillator-photomultiplier detector assembly. X-ray images recorded at energies just below and at the Fe 2p (700, 709.5 eV) and C 1s (280, 305 eV) absorption edges were converted into optical density (OD) images and used to derive the corresponding elemental maps. Carbon 1s and Fe2p NEXAFS spectra from regions of interest were obtained from image sequences (i.e., stacks) collected at energies spanning the relevant absorption edge (280–305 eV for C, 700–730 eV for Fe). At least two different sample regions were analyzed for each element. Theoretical spatial and spectral resolutions were 30 nm and ±0.1 eV, respectively. All measurements were performed at ambient temperature and <1 atm He. Calibration at C 1s edge was accomplished with the 3s (292.74 eV) and 3p (294.96 eV)

Table 3

Fe, Mn, Cu, Zn, and S minerals identified by Fe 1s XANES spectroscopy and X-ray diffraction.

Minerals		Identification
Sulfides (15)		
<u>Pyrrhotite</u> ^a	Fe _(1-x) S x = 0–0.2	XRD ^b , Fe XANES ^c
Unidentified	FeS	Fe XANES
Mackinawite	FeS	XRD
<u>Pyrite</u>	FeS ₂	XRD, Fe XANES
<u>Bornite</u>	Cu ₅ FeS ₄	XRD
Cubanite	Cu _{0.33} Fe _{0.67} S ₄	XRD
<u>Chalcopyrite</u>	CuFeS ₂	XRD
<u>Chalcocite</u>	Cu ₂ S	XRD
<u>Covellite</u>	CuS	XRD
Digenite	Cu _{1.95} S	XRD
Fukuchilite	Cu _{0.75} Fe _{0.25} S ₂	XRD
<u>Alabandite</u>	MnS	XRD
Rambergite	MnS	XRD
Hauerite	MnS ₂	XRD
<u>Sphalerite</u>	ZnS	XRD
Oxides (6)		XRD
<u>Ferrihydrite</u>	Fe ₂ O ₃ × 0.5H ₂ O	XRD, Fe XANES
Maghemite	Fe ₂ O ₃	XRD
<u>Magnetite</u>	Fe ₃ O ₄	XRD
Crednerite	CuMnO ₂	XRD
Bixbyite	Mn ₂ O ₃	XRD
Franklinite	(Zn,Mn, Fe)(Fe,Mn) ₂ O ₄	XRD
Other phases		
Native S	S ₆ , S ₈	XRD

^a The 12 underlined minerals are predicted by geochemical modeling or closely approximated by predicted minerals.

^b Identifications based on >1 XRD peak; eight additional identifications based on 1 peak in Table S2.

^c Identifications based on >4 observations and excellent to fair matches to a Fe 1s XANES reference database (Marcus et al., 2008). Match statistics and mol fraction Fe estimates provided in Table S1.

Rydberg transitions of gaseous CO₂, and at Fe 2p edge using the main Fe 2p_{3/2} resonance of ferrihydrite set at 709.5 eV. All STXM data processing was carried out with the IDL aXis2000 software package (<http://unicorn.mcmaster.ca/aXis2000.html>).

2.5. Thermodynamic equilibrium reaction path modeling

Equilibrium thermodynamic reaction path modeling was used to predict initial O₂ and S₂ gas fugacities and the resulting mineral precipitation from mixing of seawater with each of the >250 °C, 9°N vent fluids reported by Von Damm (2000) (Tables 4 and S1). Summary results are reported for all 19 samples; results for the one sample from the 9 50' EPR area, Bio 9 vent, are also reported individually (Table 5).

Our approach followed those of previous studies (Janneycky and Seyfried, 1984; Bowers et al., 1985; McCollom, 2000). Reaction path modeling was performed with REACT and phase diagrams were produced using ACT2, both part of the Geochemist's Workbench software package (Bethke, 2007). A general limitation of REACT is that it

Table 4

Endmember data for geochemical modeling.

	Bio 9 vent ^a	Seawater
T (C)	368	2
pH ^b	3.3	8
O ₂ , aqueous	0	0.1 ^c
H ₂ , aqueous	2.8 ^d	0
SO ₄ ²⁻	0	28.0
H ₂ S, aqueous	21	0
ΣCO ₂ , aqueous	45 ^d	1.8
Cl ⁻	154	540
Na ⁺	139	464
Ca ²⁺	2.07	10.2
Mg ²⁺	0	52.2
K ⁺	3.69	10.1
SiO ₂ , aqueous	9.90	0
Fe	2.19	0
Mn ²⁺	0.29	0
Cu ⁺	0.04 ^e	0
Zn ²⁺	0.10 ^e	0
Ba ²⁺	0.01 ^e	0

All concentrations in mmol/kg vent fluid.

^a Vent chemistry data from Von Damm (2000).

^b In situ pH calculated from pH measured at 25 °C.

^c Aqueous O₂ from WOCE section P04 (Talley, 2007).

^d Dissolved gases from Proskurowski et al. (2008).

^e Based on EPR 21°N (Von Damm et al., 1985).

does not predict the thermodynamic behavior of solid solutions. Thus minerals such as sphalerite, pyrrhotite, chalcopyrite, and isocubanite are treated as separate phases with ideal stoichiometries. This may influence the predicted plume mineral assemblage.

Thermodynamic data was predicted by SUPCRT95 (Johnson et al., 1992) for the temperature range of 1–425 °C (specifically 1, 25, 60, 100, 225, 290, 350, and 425 °C) and a pressure of 500 bar, a pressure and temperature range that encompasses all known deep sea vents. SUPCRT95 uses thermodynamic data for minerals, gases, and aqueous species taken from Helgeson et al. (1978), McCollom and Shock (1997), Saccoccia and Seyfried (1994), Shock et al. (1989, 1997), Shock and Helgeson (1988), and Sverjensky et al. (1997). Thermodynamic data for pyrolusite, bixbyite, hausmannite, and marcasite were added from Robie et al. (1979) and thermodynamic data for Fe(OH)₃ were added from Wagman et al. (1982). The B-dot activity model was used (Helgeson, 1969; Helgeson and Kirkham, 1974). The temperature dependent activity coefficient for aqueous CO₂ was derived from the empirical relationship of Drummond (1981) and the temperature dependent activity of water in an NaCl solution was derived from the formulation of Bethke (2007), Cleverley and Bastrakov, (2005) provide useful temperature dependent polynomial functions for both these last two parameters.

Inorganic vent fluid composition was based on the measurements of Von Damm (2000) with the exception of Cu, Zn, and Ba, which for lack of synoptic data, were based on measurements from EPR 21°N (Tables 4 and S3; Von Damm et al., 1985). Endmember gas chemistry concentrations are based on the data reported by Proskurowski

Table 5
9°N modeled maximum plume mineral concentrations.

Mineral	9°N region ^{a,b}		Bio 9 vent ^c mmol/kg _{vent fluid}
	mg/kg _{vent fluid}	mmol/kg _{vent fluid}	
Anhydrite	CaSO ₄	720 ± 330 ^d	5.3 ± 2.4 ^d
SiO ₂ , amorph.	SiO ₂	4 ± 8	0.063 ± 0.014
Barite	BaSO ₄	0.9	0.004
native S	S	910 ± 720	28 ± 22
Fe-hydroxide	Fe(OH) ₃	230 ± 150	2.1 ± 1.4
Pyrite	FeS ₂	270 ± 160	2.2 ± 1.4
Magnetite	Fe ₃ O ₄	140 ± 110	0.610 ± 0.460
Pyrrhotite	FeS	5 ± 10	0.054 ± 0.130
Chalcopyrite	CuFeS ₂	7.5	0.041
Covellite	CuS	3.8	0.040
Bornite	Cu ₅ FeS ₄	4.1	0.0081
Chalcocite	Cu ₂ S	1.4	0.009
Pyrolusite	MnO ₂	42 ± 47	0.49 ± 0.54
Alabandite	MnS	3 ± 7	0.029 ± 0.084
Sphalerite	ZnS	10	0.1

^a Summary results for 19 vent samples (263–403 °C) from 9°N EPR (Von Damm, 2000).

^b Results are based on the maximum plume mineral concentration for each phase; many dissolve to reform other minerals in this list, so results should not be totaled.

^c B9 is the one sample of the 19 that is also in the 9°50'N EPR area.

^d 1σ variability estimate, except for Ba, Cu, Zn due to limited data.

et al. (2008). *In situ* pH was calculated from measurements of pH at 25 °C using an equilibrium reaction path model that increased the temperature of measured fluid to the original vent fluid temperature. Note, this available data predates the most recent eruption at this site and is only used as an example of East Pacific Rise chemistry. Actual vent chemistry at the time of this study may well have been different.

The modeled thermodynamic equilibrium reaction path followed the mixing of 1 kg of high temperature vent fluid with 2 °C seawater to plume dilutions of 1:10,000. Following assumptions used in previous models, conductive cooling was neglected and mixture temperatures were a strict function of conservative end-member mixing (Janecky and Seyfried, 1984; Bowers et al., 1985; McCollom, 2000). Also, following assumptions used in previous models, HS[−]/SO₄^{2−} equilibration was suppressed on the basis that this reaction is kinetically inhibited on the short timescales of transport in the rising plume where it is energetically favored. The precipitation of hematite was suppressed to allow Fe hydroxide to precipitate on the basis that the latter is a closer approximation than the former to the more common amorphous Fe oxyhydroxides, which precipitate preferentially due to kinetic effects. The precipitation of Mg bearing minerals, and silicates, with the exception of amorphous silica, was also suppressed for simplicity. Some in this group have been found as minor plume constituents, others such as quartz appear kinetically inhibited; but in any case, the suppression of this group does not influence the precipitation of the Fe, Cu, or Mn minerals of interest in this study.

Precipitated minerals were allowed to dissolve and their constituents to re-precipitate based on thermodynamic equilibrium constraints. Consequently, a summation of minerals present at any point in the reaction path would

only represent a subset of all minerals that precipitate during the process. Therefore, to summarize all of the minerals that precipitate during the reaction path, the maximum mineral concentration for each phase is reported (Table 5). These values can be mutually exclusive (e.g., pyrite, magnetite, and Fe hydroxide) and should not be totaled.

2.6. Particle settling calculations

Particle settling velocity estimates for aggregated plume particles and their unaggregated organic and inorganic constituents are based on Stokes' equation: $w = g[\rho_p - \rho_f]D_a^2(18\eta)^{-1}$, where w is the settling velocity, g is the acceleration of gravity, ρ_p is the density of the aggregate, mineral grain, or floc particle; ρ_f is the density of seawater, D_a is the effective diameter of the aggregate, and η is the dynamic viscosity of seawater. Values of 9.81 m s^{−2}, 1035 kg m^{−3}, and 1.567×10^{-3} kg m^{−1} s^{−1} were used for g , ρ_f and η ; assumptions concerning ρ_p and D_a are presented in Section 4.3.

3. RESULTS & DISCUSSION

Optical backscatter profiles collected before and after the deployment are consistent with the sampler remaining within the plume during the timeseries (Fig. 1d). During this period, the along axis current (v) at this location was characterized by a speed of ~2–5 cm s^{−1} and predominantly northward direction. There was one episode of southward flow, lasting approximately 12 h, toward the end of the sampling period. The cross-axial current (u), on the other hand, was dominated by the semidiurnal tide and associated with peak speeds of ~10 cm s^{−1}. As a result of the predominantly northward along-axis flow, the most likely sources of the hydrothermal material in the SUPR

samples are vents to the south, the most proximal being the Bio9 and P vents. Given the distance between these vents and the SUPR sampler, and the observed along axis velocities we infer typical transport times from 1 to 4 h between expulsion at the vent orifice and collection at the sampler. The cross axis tidal flows imply the SUPR sampler was not always directly in the dispersing plume of the Bio9 and P vents; in such cases any hydrothermal material collected would then be significantly but indeterminately older either having recirculated with the currents or sourced from vents even further south.

3.1. Sampling system performance

This was the first study to make use of the SUPR sampling equipment, the development of which was reported previously (Breier et al., 2009). As designed, the volume of water filtered varied in response to the demand placed on the filtering system. Variability in sample volumes over the 3-day time-series deployment was high, ranging from 3 to 97 L (Table 1). This suggests filtration of plume waters with varying particle concentrations and/or size distributions; the latter may have been particularly important because the most visibly loaded filters (i.e., samples 2 and 22, which were for detailed analysis) also achieved the greatest filter volumes. This would be consistent with collection of coarse-grained particles that were retained by, but did not clog, the filter membranes.

3.2. Bulk geochemistry of the nonbuoyant plume

All of the samples analyzed for this study, with the exception of one, were predominantly hydrothermal in origin as indicated by $\text{Al}/(\text{Al} + \text{Fe} + \text{Mn})$ ratios <0.5 (Table 1). The $\text{Al}/(\text{Al} + \text{Fe} + \text{Mn})$ ratio, which we will refer to subsequently as the Hydrothermal Index (HI), has been used as an indicator of the relative contribution of hydrothermal and detrital sediment sources: particle mixtures with a greater hydrothermal component are enriched in Fe and have lower HI values (e.g., Boström and Peterson, 1969). For example, background particles in the 9°N EPR area have a HI value of 0.8 (Sherrell et al., 1999). The outlier in this study, sample 1, had a HI value of 0.96; but this was due to an unusually high Al concentration of 222 nM that we consider an indication of contamination, thus this sample is excluded from subsequent discussion. The observed ratios in this study show variability in the hydrothermal component of these EPR plume particle samples (Fig. 2). A sequence of four low volume samples (Table 1: 15, 16, 18, 19) had HI values <0.09 with Al concentrations near or below the detection limit. These low values are indicative of a period of time when particles within the plume are essentially all hydrothermally derived. The average HI value over the three days was 0.3 (range: 0.05–0.48), with a slightly decreasing trend observed over the course of the deployment. These values are consistent with previous measurements for EPR 9°N plumes (0.1–0.3; Sherrell et al., 1999).

Iron concentrations for these $>1 \mu\text{m}$ particulate samples ranged between 0.5 and 13 nM (Table 1), and are less than

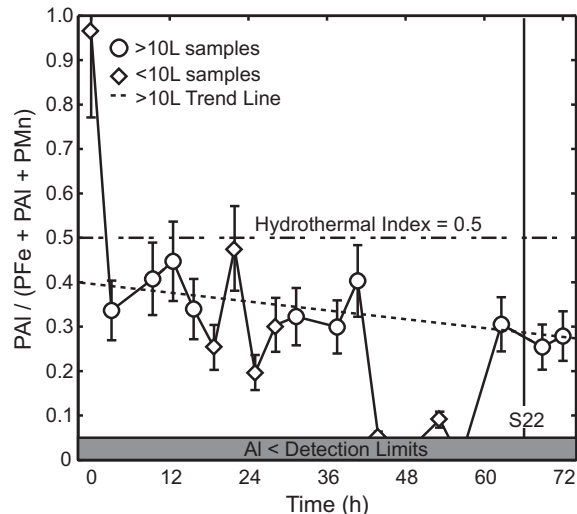


Fig. 2. Plot of Hydrothermal Index (HI) values ($\text{Al}/(\text{Al} + \text{Fe} + \text{Mn})$; Boström and Peterson (1969) for particulate samples collected over a 72 h time-series above the EPR 9°50'N. Lower HI values (<0.5) are indicative of a dominant hydrothermal input. This time-series illustrates the variability of the hydrothermal component in near-field plume particles at 9°50'N EPR. During the 72 h span there was one sustained excursion to extremely low HI values (and concomitantly low volumes of water filtered prior to clogging) that was sustained for ~ 12 h, superimposed upon a decreasing trend in HI values for samples in which volumes >10 L were filtered. The sequential position of sample 22, which was reserved in whole for STXM, is indicated by a vertical dashed line instead of a symbol due to the absence of bulk chemical data.

concentrations measured previously at 9°45'N EPR for $>0.45 \mu\text{m}$ particulate samples (10–56 nM: Sherrell et al., 1999; Field and Sherrell, 2000). These differences are consistent with the fact that previous measurements include the $0.45\text{--}1 \mu\text{m}$ particle size class not collected in this study. Sands et al. (2012) report on particle size partitioning for trace elements including Fe in hydrothermal plumes from the Edmond vent field in the Central Indian Ocean. In that case, the $0.1\text{--}0.4 \mu\text{m}$ particle size class represented 50% of total Fe; though the $>1 \mu\text{m}$ particle size class was not measured it must have represented a minority of total Fe. The lower Fe concentrations measured in this study may also reflect the slow speed of dissolved Fe oxidation (Field and Sherrell, 2000), which predicts that plume particulate Fe hydroxide concentrations should be low closest to a vent and only increase with plume age and distance as they disperse down-plume from their source. In this study, all sample collection was conducted within 250 m of the Bio 9 and P vents, whereas the samples reported by Sherrell et al. (1999) and Field and Sherrell (2000) were all collected more distant (300–2000 m) from any vent-source. In addition, Mn particulate concentrations co-vary with respect to Fe with a R^2 value of 0.85 for the >10 L samples; a relationship that extends to all but one of the <10 L samples (Table 1, sample 8). Thus the relationships between trace elements and Fe reported in the remainder of this section apply nearly as well to trace elements and Mn.

Phosphorus, V, As, and Cr share common traits of forming oxyanions in seawater and being scavenged

efficiently by Fe oxyhydroxide bearing particles (Trocine and Trefry, 1988; Feely et al., 1990, 1991; German et al., 1991b). Previous studies have shown that within hydrothermal plumes, the relationships between these elements and Fe are positive and highly linear (Feely et al., 1990, 1991; German et al., 1991b). Similar to Fe, the concentrations of P, V and As concentrations are less than previous EPR measurements, while the Cr concentrations are slightly greater (Feely et al., 1994). However, all four of these elements show positive relationships with particulate Fe contents (Fig. 3). Particularly striking linear correlations are observed for the >10 L filtered samples. The R^2 values for each of P, V, As, and Cr with respect to Fe are 0.94, 0.99, 0.95, and 0.60, respectively, and their molar ratios with respect to Fe are 0.06, 0.002, 0.001, and 0.06. For P, V, and As these molar ratios are, to varying degrees, less than previous measurements from the EPR. The P:Fe ratio of 0.055 is at the low end of the range observed in plumes to date (Feely et al., 1998), and directly comparable to the Azores area plumes of the Mid-Atlantic Ridge (Edmonds

and German, 2004). By contrast nonbuoyant plume samples collected along the EPR from 8°40' to 11°50'N in 1991 had an average P:Fe ratio of 0.18 (Feely et al., 1994). The V:Fe ratio of 0.002 is less than the previous EPR average of 0.0038, but very close to the ratio of 0.0023 observed for plumes along the Juan de Fuca Ridge (Feely et al., 1992). Plumes of the Mid-Atlantic Ridge have typical V:Fe ratios >0.0040 (German et al., 1991b). The As:Fe ratio of 0.00096 is approximately half the value of previous measurements, which have typically been close to 0.002 (German et al., 1991b; Feely et al., 1992). Conversely, the Cr:Fe molar ratio of 0.059 is significantly greater than previous measurements, which for EPR were 0.001 and for the TAG site at the Mid-Atlantic Ridge were 0.0008 (German et al., 1991b; Feely et al., 1994).

Dissolved REEs in seawater are also scavenged by hydrothermal plume particles (Klinkhammer et al., 1983; German et al., 1990). Our samples exhibit characteristics that are typical of hydrothermal plume particles: variable enrichments in Sm, Eu, and Gd and Ce-anomalies that are positive with respect to seawater dissolved REE concentrations and negative with respect to Post Archean Australian Shale (PAAS) composite REE concentrations (Table 2), (Taylor and McLennan, 1985; Rudnicki and Elderfield, 1993; Sherrell et al., 1999). The degree of enrichment due to hydrothermal scavenging is modest compared with previous EPR plume and sediment trap samples, but enrichments in Sm, Eu, and Gd and negative Ce-anomalies with respect to PAAS are observable (Fig. 4a). The background aluminosilicates mixed with the hydrothermal material in these samples undoubtedly also contribute a significant shale-like fraction to the total LREEs reported here. To highlight the seawater scavenging pattern, the aluminosilicate background can be removed by first normalizing the sample LREE concentrations to the sample Al content, subtracting similarly Al-normalized background LREE concentrations, and normalizing to dissolved Pacific seawater LREE concentrations (Alibo and Nozaki, 1999; Sherrell et al., 1999). In this case, we have no true background sample and have instead used sample 5, with the highest HI value, as the closest approximation to background. Even though this results in an over-correction, the seawater scavenging pattern remains clear (Fig. 4b). With one exception, the LREE pattern of the >10 L particle samples is consistent with the primary LREE source being the seawater dissolved pool and not vent fluids, which exhibit a prominent, positive Eu-anomaly (Klinkhammer et al., 1994). The exception is sample 14, which has an unusually high Eu-anomaly, this may represent an interference from ^{137}Ba / ^{16}O , but potentially reflects a contribution from sulfides enriched in vent fluid derived REEs, which have a pronounced positive Eu anomaly (Byrne and Sholkovitz, 1996).

The primary difference in the REE pattern between these samples are the Ce-anomalies, which arise because, unlike its trivalent neighbor REEs, Ce(III) can be readily oxidized to highly insoluble and oxide forming Ce(IV). For the >10 L filtered particulate samples, the REE patterns are very similar to those identified previously for plume particles at 9°45'N EPR by Sherrell et al. (1999) and in sediment

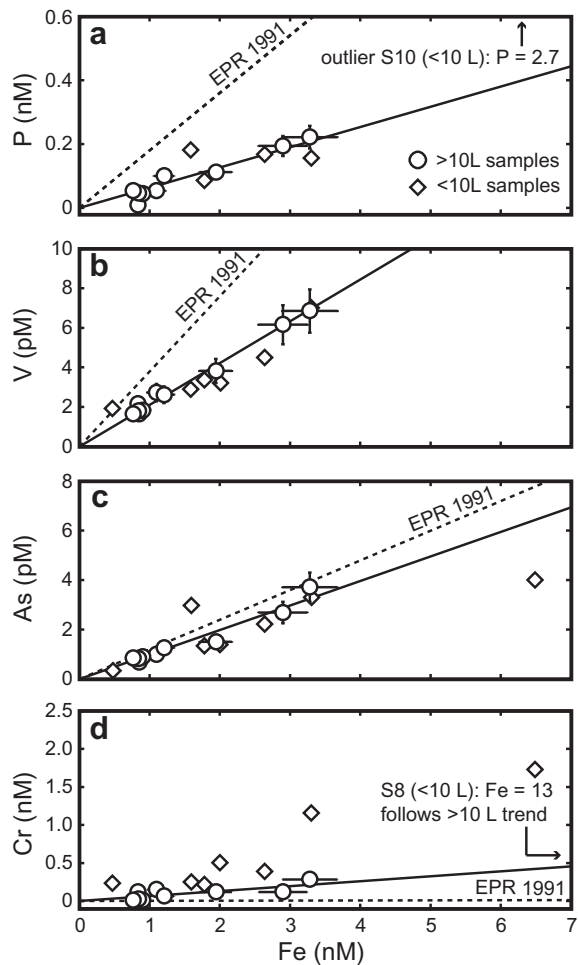


Fig. 3. Particulate concentrations of P, V, As, and Cr plotted versus particulate Fe concentrations for the nonbuoyant buoyant plume samples; linear regression trends (forced to 0) for the >10 L samples are also plotted. For comparison, the linear regression trends (forced to 0) are also shown for the EPR 1991 samples of Feely et al. (1994).

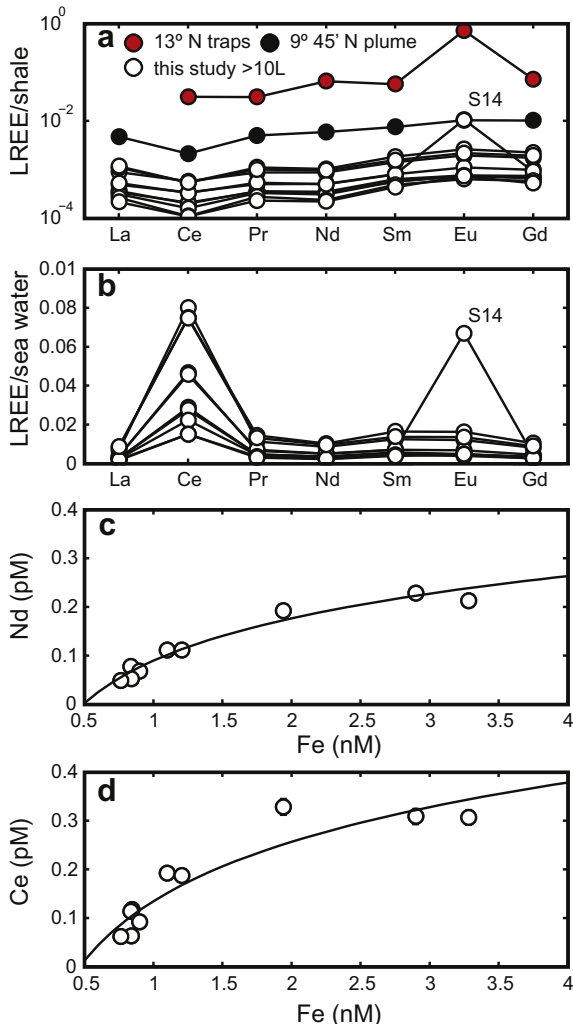


Fig. 4. (a) Shale (PAAS) normalized particulate LREE concentration patterns for the time-series plume samples collected in this study, the average of 9°N region plume samples collected by Sherrell et al. (1999), and the average of 13°N EPR near field sediment traps collected by German et al. (2002); (b) background corrected, seawater normalized, particulate LREE concentration patterns; and plots of particulate (c) Nd and (d) Ce concentrations versus particulate Fe for the EPR nonbuoyant buoyant time-series samples.

traps at 13°N EPR by German et al. (2002); but in this case the enrichments relative to seawater are less by factors of 10 and 100, respectively (Fig. 4a). Part of this lower enrichment is potentially due to the fact that uptake of REEs by Fe oxyhydroxides is a continuous scavenging process. For this reason, the anticipated REE/Fe ratios of hydrothermal plume particulates are also anticipated to increase progressively as plume particles are dispersed through the water column and into the underlying sediments, as was the case for particulate Fe concentrations (Ruhlin and Owen, 1986; Owen and Olivarez, 1988; Olivarez and Owen, 1989; German et al., 1990, 1997; Edmonds and German, 2004). Consistent with those earlier studies, the trends for our samples of particulate REE versus particulate Fe also show a marked positive curvature (Fig. 4c and d) that is

quite distinct from the positive linear relationships observed between Fe and P, V, As, and Cr (Fig. 3).

3.3. Particle-by-particle geochemistry in the nonbuoyant plume

Sample 22 was reserved for particle-by-particle geochemical analyses. This sample is bracketed in time by samples with HI values near the 3 day average of 0.3 and we assume this sample follows the same general biogeochemical trends and patterns as those other large-volume samples. We do not, however, assume that this sample represents *all* hydrothermal particles in our sample set or beyond. Nevertheless, this sample *does* represent the particles filtered from 97 L of nonbuoyant plume water, and also has characteristics consistent with sediment trap samples from this location (Toner et al., 2009, 2012). Thus, all available evidence suggests that sample 22 does not represent a rare condition and may, rather, be representative of chronic processes in the 9°50'N EPR plume.

Particle aggregation in the sample was common (Figs. 5a, 6 and, S1 and S2). We cannot completely eliminate the possibility that this aggregation is an artifact of *in situ* filtration, which must result in some degree of artificial aggregation and disaggregation. However, the observed aggregates match those from sediment trap samples from this same area from a different time period (Toner et al., 2009; Figs. 6 and S2). This suggests a common *environmental* (i.e., natural) aggregation mechanism because the collection methods employed in these two studies were quite disparate. Sediment trap sampling involves minimal physical disruption but possible diagenesis during the elapse time (order of months) between sample collection and trap mooring/recovery. By contrast, *in situ* filtration involves potentially significant physical disruption at the time of sample collection but little scope for diagenesis thereafter. Moreover, there are numerous examples in sample 22 of Fe mineral grains with closely conforming C “halos” indicative of organic surface coatings (e.g., Fig. 6, region 1, top left, 2 μm mineral grain); these features appear to be the result of environmental processes rather than artificial ones. Thus, while some sampling artifacts are likely present, the combined observations from this and the previous studies of Toner et al. (2009, 2012) indicate a natural aggregation mechanism.

A wide distribution of particle/aggregate sizes were observed but a statistical analysis of particle size was not practical within this study. Mineral grains within the plume aggregates range from less than 20 nm to greater than 10 μm in diameter. Aggregates were typically of the 10 μm scale. The particle aggregates were composed of minerals embedded in a C-rich matrix (Fig. 6). X-ray fluorescence elemental mapping indicates that these particle aggregates are primarily S-rich flocs with dimensions up to several hundred microns in length (Fig. 5a).

The geochemical speciation of the major mineral forming elements, Fe, Mn, and S, within the particles is complex. Iron oxyhydroxides, pyrite, pyrrhotite, and an unidentified, potentially amorphous, Fe monosulfide phase account for >80% of the Fe mol fraction measured by Fe 1s XANES

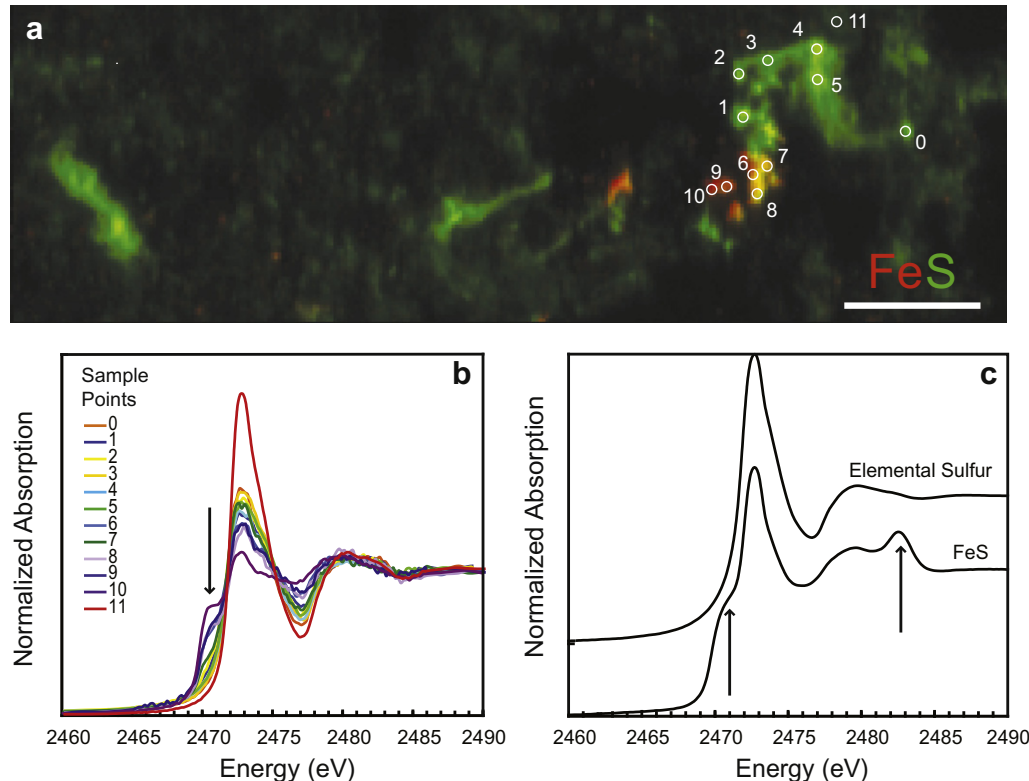


Fig. 5. Spatial distribution and valence state of S in nonbuoyant plume aggregates. (a) Sulfur and Fe distribution in particle aggregates obtained by μ XRF mapping. Bicolor coded XRF map shows S-rich areas in green and Fe-rich areas in red. Scale bar is 370 μ m. Sulfur 1s XANES spot locations are indicated by white numbers 0–11. (b) Sulfur XANES spectra of spots 0–11 along with (c) reference spectra from elemental S (S^0) and FeS (S^{2-}). The data show that nonbuoyant plume aggregates are composed of S^0 as well as compound(s) having a lower S oxidation state (S^{1-} , S^{2-}). However, spectral signatures are different from FeS or pyrite. Iron 1s XANES spectra recorded on these 12 locations (and others) were also recorded (not shown).

spectroscopy; but Fe is observed in >10 different species as identified by both XRD and Fe 1s XANES (Tables 3 and S1). Measurements by Fe 1s XANES and XRD support 22 mineral phases (Table 3) and another eight are suggested by 1 peak XRD identifications (Table S2). Single-phase Fe-bearing particles were rarely observed; only one spectrum supported a pure pyrite particle, all others were two or more Fe-bearing phases within the same aggregate. Particulate Mn was prevalent in the plumes in both oxidized and reduced mineral phases: Mn sulfides (alabandite, with haueite and rambgerite suggested) and Mn oxides (bixbyite, with hausmannite and pyrolusite suggested) (Tables 3 and S2). The valence state of S in particle aggregates, as measured by S 1s XANES spectroscopy, is reduced with all values falling between S^0 and S^{2-} (Fig. 5b and c).

The As and V distributions within the particles and aggregates were determined by XRF mapping (Fig. 7) and XRF spectroscopy at single points. Arsenic and V were associated with both Fe oxyhydroxides and sulfides but not uniformly. Iron oxyhydroxides were observed to have: (1) no detectable As or V; (2) As only; or (3) both As and V. All pyrite-rich particle/aggregates contained As, only one such particle/aggregate contained both As and V. Particle/aggregates with high As counts were positively correlated with Zn and Fe. Vanadium was distributed as small discrete particles within larger aggregates, and appears to be correlated with

Mn in many cases (see V, S, Mn maps, Fig. 7). The speciation of As and V was not determined for this study.

A pervasive particulate organic matrix is observed in the nonbuoyant plume at EPR 9°N (Figs. 6 and S2). Research at 9°50'N EPR has shown that particulate organic matter is expulsed from the seafloor (Haymon et al., 1993), enriched in the nonbuoyant plume (Bennett et al., 2011), and collects in sediment traps (Toner et al., 2009). Our results reveal how that material is aggregated with mineral particles (Fig. 6). The organic matrix is pervasive, fibrous and rich in C. Carbon 1s XANES spectra exhibit peaks typical of peptide bonds in protein amide groups (288.2 eV, $1s \rightarrow \pi^*_{C=O}$ transition) and carboxyl or ester groups (288.4 eV, $1s \rightarrow \pi^*_{C=O}$ transition) (Fig. 8; Stöhr, 1992; Cody et al., 1998; Boyce et al., 2002). Other functional groups detected include unsaturated or aromatic C, and oxygenated organic functional groups, aliphatic-C, aromatic carbonyls or aromatic hydroxyls (~ 285.1 eV, $1s \rightarrow \pi^*_{C=C}$ transitions; ~ 287.3 eV $1s \rightarrow \sigma^*$ broad shoulder; Myneni, 2002; Brandes et al., 2004; Solomon et al., 2009). These data show the organic nature of the matrix, with functional group signatures consistent with biomolecules (Figs. 6 and 8).

The nanoscale distribution of Fe within particle aggregates is strongly correlated with C (Figs. 6 and S2). Within the particle aggregates Fe speciation is a mixture of Fe(II)

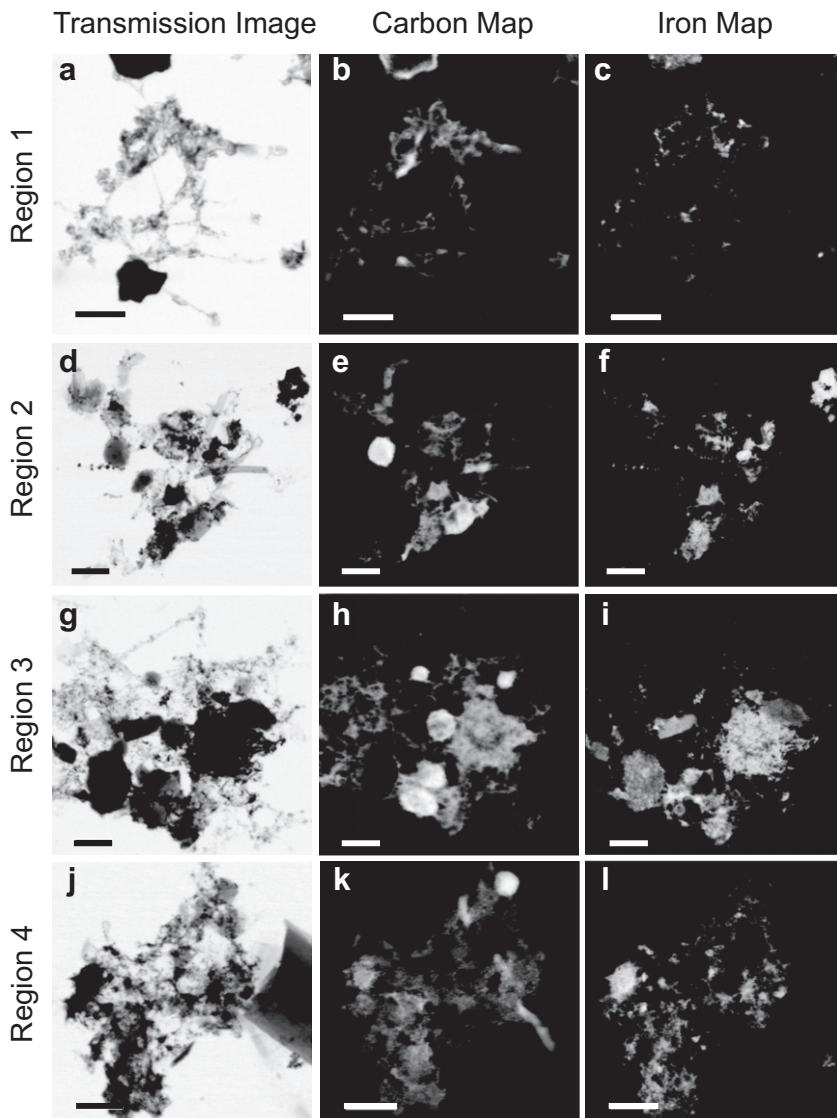


Fig. 6. Examples of particle aggregation in the nonbuoyant plume. Scanning transmission X-ray microscopy images (a, d, g, j), distribution maps of C (b, e, h, k), and Fe (c, f, i, l). All scale bars are 2 μm .

and Fe(III), and particles with <20 nm diameter having spectral features consistent with Fe(III) oxyhydroxides (Chan et al., 2009) were observed frequently (Figs. S3 and S4). Although less frequently observed than Fe(III) at this spatial scale, Fe(II) is correlated with C in aggregates (e.g., Fig. S3, spectrum a12). This is also in agreement with sediment trap samples from this area (Toner et al., 2012). Spectral signatures for Fe sulfides were rarely encountered during STXM analyses, i.e., pyrite is observed as larger particles with X-ray microprobe, which are too thick (optical density saturated) to provide reliable XANES spectra.

3.4. Geochemical modeling of mineral formation in the nonbuoyant plume

Our goal in this section is to determine the extent to which non-equilibrium mechanisms need to be considered in the plume mineral formation process – by comparing

predictions based on equilibrium reaction path modeling against observed mineral phases. The modeling results cannot be considered definitive because (i) we do not know the vent chemistries at the times our samples were collected, (ii) stoichiometry of the reactions is uncertain, and (iii) kinetic inhibitions are probable. Plume mineral formation and dissolution were modeled for the 19 EPR high temperature vent fluids described by Von Damm (2000) including Bio9, one of the “Hole to Hell” vents. Each reaction path was followed to a plume dilution of 1:10,000 and a final mixture temperature of 2 °C (Lupton et al., 1985).

In total, 29 mineral phases are supported or suggested by measurements made on sample 22; 12 of these phases were predicted to occur by thermodynamic modeling at various points in 9°16'–9°50'N vent plume reaction paths or were closely approximated by predicted phases (Table 5); 15 phases had no close match in the thermodynamic database and cannot be predicted; and 1 phase (hausmannite)

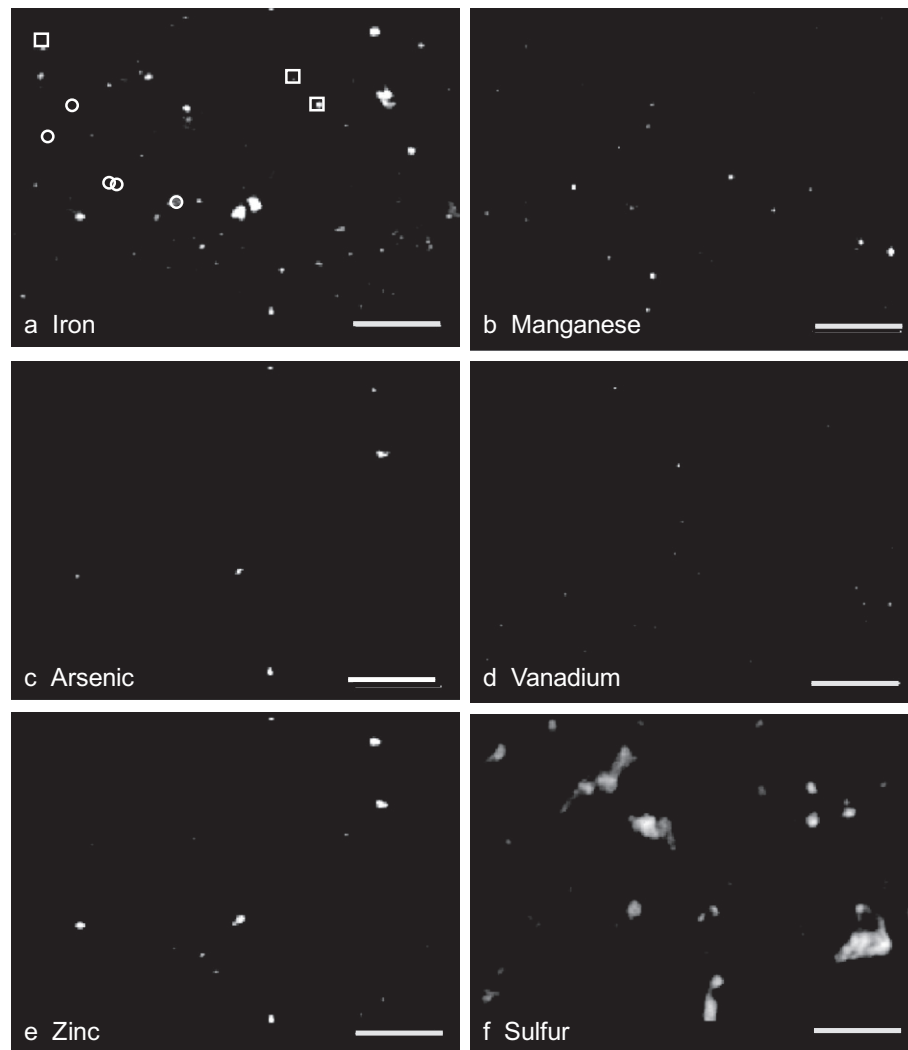


Fig. 7. Elemental distributions of Fe, Mn, As, V, Zn, and S in nonbuoyant plume aggregates. For the Fe map, particles with white squares are predominantly pyrite, and those with white circles are predominantly Fe oxyhydroxide. Scale bar is 300 μm .

suggested by a single Bragg peak in XRD measurement was not predicted to form (Table 3 and S2). The observations show that a diverse assemblage of Fe, Cu, and Mn oxides and sulfide phases can exist together in the nonbuoyant plume, even in the same aggregates. This observed mineral assemblage, when compared with equilibrium thermodynamics predictions, represents a state of thermodynamic disequilibrium. Using the reaction path for Bio 9 as an example, thermodynamic equilibrium constraints predict that the initial major Fe sulfide phase, pyrite, will be replaced by magnetite, which will be replaced by Fe hydroxide phase. In this example, pyrrhotite only precipitates if pyrite and marcasite formation are suppressed (Fig. 9). All of the minerals just mentioned are observed in sample 22. Vent chemistry does vary between vents and with time, and due to the proximity of several phase boundaries, it is likely the mineral formation process does as well (Fig. 10), but none of the vent fluid chemistries we modeled produces a mineral assemblage that significantly alters this comparison between observed and predicted mineralogy (Table 5). Sander and Koschinsky (2011) report that hydrothermal

metals can be stabilized as organic-metal complexes; for example, as much as 4% of hydrothermal Cu may undergo organic complexation. This is not accounted for in our predictions, and would lower the availability of dissolved metals for these mineral forming reactions; thus decreasing predicted amounts and modifying the relative mineral abundances. Additional factors that may account for the discrepancies between observed and predicted mineralogy include conductive cooling of the plume, kinetic inhibitions in formation and dissolution reactions, deviations from idealized stoichiometry, stabilization of mineral phases by size effects, microbial processes, and stabilization of mineral phases by aggregation with organic material.

4. SYNTHESIS AND IMPLICATIONS

4.1. Geochemical and temporal variability of hydrothermal plumes

The geochemical observations made for this study are indicative of a variable and heterogeneous particle field

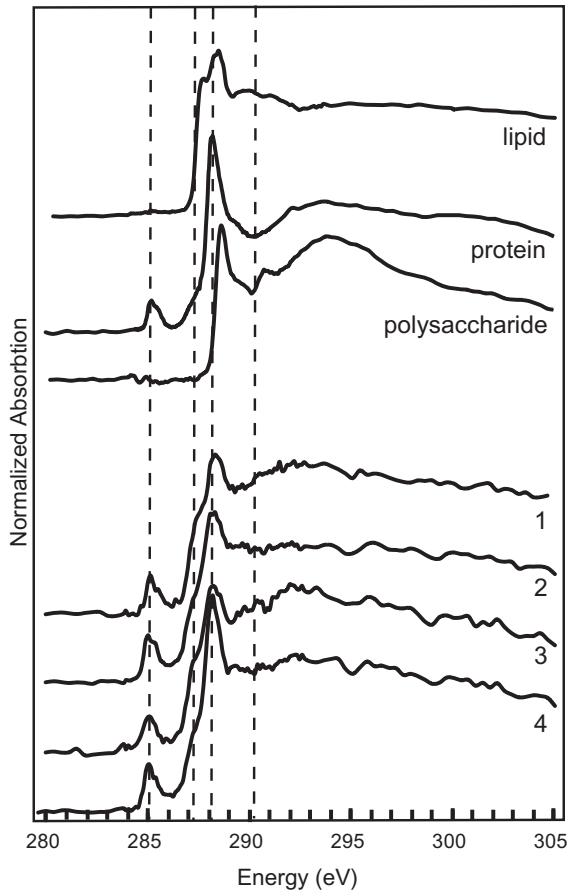


Fig. 8. Summary of C 1s XANES spectra from representative of nonbuoyant plume aggregates. Reference spectra: lipid (1,2-dipalmitoyl-sn-glycero-3-phosphoethanolamine); protein (bovine serum albumin); polysaccharide (alginate). Indicative vertical dashed lines are: 285.2 eV for $\pi^*(C=C)$ of unsaturated or aromatic C; 287.3 eV for σ^* of aliphatic C, aromatic carbonyl, aromatic hydroxyl, other oxygenated groups; 288.2 eV for $\pi^*(C=O)$ of amide (peptide bond); and 290.3 eV for $\pi^*(C=O)$ of carbonate (Sandford et al., 2006; Cody et al., 2011).

within the nonbuoyant plume at this location, depth, and time-scale. Bulk geochemistry (Fig. 2), mineralogy (sulfides), and CTD optical backscatter profiles before and after the deployment (Fig. 1d) are consistent with the sampler remaining within the plume during the deployment. However, changes in hydrothermal input were observed (Fig. 2). As the hydrodynamics of buoyant and nonbuoyant plumes are complex, the observed variability is reasonable. However, at these short time-scales the bulk characteristics of plumes have been poorly constrained because the primary source of time-series information to date is derived from sediment traps (e.g., Dymond and Roth, 1988; Khripounoff and Alberic, 1991; German et al., 2002; Khripounoff et al., 2008). Based on our observations, some of the temporal variability in the hydrothermal component of these samples is likely related to the variable currents at this location.

The most striking indicator of heterogeneity within the nonbuoyant plume is the speciation of the major mineral forming elements: Fe, Mn, and S. Iron, Mn, and S were

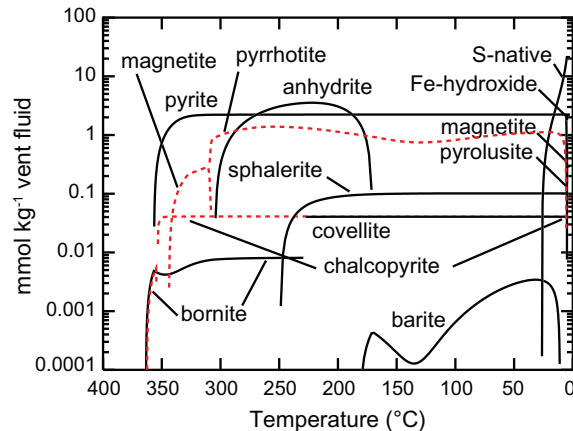


Fig. 9. Thermodynamic equilibrium modeling predictions for the mineral precipitation resulting from the convective mixing of 1 kg of Bio 9 vent fluid to a plume dilution of 1:10,000 and a final mixture temperature of 2°C. Suppression of pyrite and marcasite reactions permits pyrrhotite precipitation.

all observed in oxidized and reduced phases in the same sample, representing a narrow window in time and space, within the young nonbuoyant plume. The simultaneous presence of reduced and oxidized species, particularly unexpected phases such as highly soluble Mn sulfides, in the nonbuoyant plume at EPR requires some combination of kinetic limitations, metastability, or organic coatings to preserve, or slow dissolution of the reduced phases that form in the lower plume. The short transport time from source to point of collection (a few hours) and observations of aggregation make any of these factors reasonable.

4.2. Particle mineralogy and trace element reactivity

A diversity of Mn, Fe, Cu, and Zn sulfide and oxide minerals were observed in the nonbuoyant plume, many of which are consistent with previous observations (pyrrhotite, pyrite, chalcopyrite, bornite, and magnetite; Mottl and McConachy, 1990). However, we did observe minerals not previously identified in hydrothermal plumes, and many are presently not available in existing thermodynamic databases used with equilibrium speciation programs (e.g., EQ3/6 and Geochemist Workbench). The major minerals observed are generally consistent with the phases predicted by equilibrium thermodynamic modeling but a detailed comparison reveals important differences with respect to mineral stability and trace element uptake. Thermodynamic databases and thus thermodynamic equilibrium reaction path modeling results are biased toward more stable, higher crystallinity phases. Therefore, predicted mineral assemblages can differ from real world assemblages both in terms of composition and mineral diversity. When mixing along the reaction path is as rapid as it is in the rising plume, a disequilibrium assemblage of phases must be expected. These results highlight the degree of complexity in the trace mineralogy of EPR plume particles and have implications for the transport of major, minor, and trace elements associated with plume material.

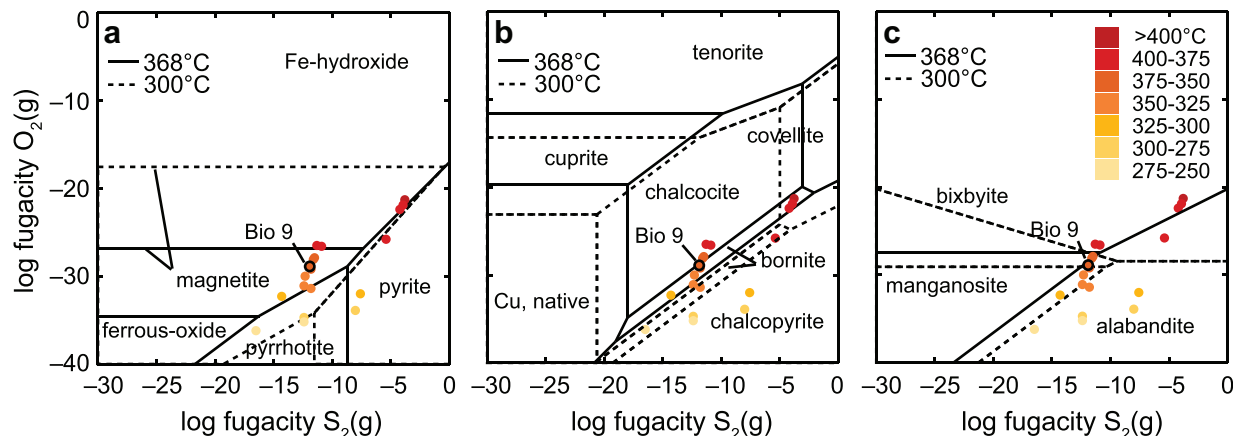


Fig. 10. Equilibrium phase diagrams on the basis of logarithmic $O_2(g)$ and $S_2(g)$ gas fugacities for the (a) Fe–S–O, (b) Cu–Fe–S–O, and (c) Mn–S–O systems at 500 bar. Solid lines represent 368 °C phase boundaries. Dashed lines represent 300 °C phase boundaries. An open circle represents the initial state of Bio 9 vent fluid (368 °C). Solid circles represent the initial $O_2(g)$ and $S_2(g)$ gas fugacities of the other >250 °C, 9°N vent fluids reported in Von Damm (2000); these fluids span a broad temperature range and are only shown to indicate their general relationship to the phase transition zones. Only the relationship between Bio 9 and the 368 °C phase boundaries can be interpreted literally. Marker color corresponds to endmember vent fluid temperature.

Past treatments of trace element uptake by co-precipitation and surface adsorption, and release by dissolution, focused on the general processes common to the two major mineral classes: sulfides and Fe oxyhydroxides (Rudnicki and Elderfield, 1993). Phosphorus, V, As, and Cr form oxyanions in seawater, and the presence of these trace elements in hydrothermal particulate samples has been attributed to uptake by hydrothermal plume Fe oxyhydroxides (Trocine and Trefry, 1988; Feely et al., 1990, 1991; German et al., 1991b). The positive linear correlation between P, V, As, and Cr with Fe in plume particulates observed here (Fig. 3) is in agreement with previous studies (Feely et al., 1990, 1991; German et al., 1991b). However, particle-by-particle measurements of As and V content in these samples indicate that trace element incorporation by individual mineral particles is nonuniform despite positive linear correlations in the bulk. For As, at least two mineral populations are observed in the nonbuoyant plume in this study: As–pyrite and As–ferrihydrite. The mechanisms of trace element uptake in plumes that lead to the observed bulk As:Fe ratios have not been identified, and may be more complex than mineral surface adsorption from seawater. In fact, the “lock-in” of molar ratios like P:Fe, V:Fe, As:Fe, and Cr:Fe implies a mechanism that differs from continuous surface adsorption as for the REEs, Y, Be, and Th (German et al., 1991a,b). Understanding the mechanisms and phases involved in processes like these are important when considering the transport and fate of these elements. For instance, the As we observe in the sulfide minerals may be from the vent fluids and subject to dissolution and release to seawater. Certainly, existing elemental data, alone, cannot confirm to what extent this occurs or to what extent it would be balanced by Fe oxyhydroxide uptake. However, the bulk and particle-specific geochemical observations reported here illustrate that dynamic heterogeneous chemical reactions may be masked by the relatively straightforward appearance of element versus element correlations. This may seem counterintuitive, but it only

requires that the scavenging mineral assemblage have a consistent ratio. This may be the case for these samples, which were collected from a fixed point close to a source vent.

It should also be noted that the causal mechanisms for the linear relationships we observe in this study are not necessarily the same as for linear relationships observed in previous studies (e.g., Feely et al., 1998). Previous studies that identified amorphous Fe hydroxides as primary scavengers were inclusive of nonbuoyant plumes over much larger spatial scales and consequently larger particle age ranges. However, at the shorter scales of this study, amorphous Fe hydroxides only represent a fraction of particulate Fe (Table S1, 24%). Thus, the trends observed in this study may represent processes prior to significant Fe hydroxide scavenging; processes that may set the initial baseline for particulate trace element concentrations in plumes.

4.3. Particle morphology, aggregation, and transport

Mineral aggregation by organic material appears to be pervasive in both nonbuoyant and settling plume particles examined from this site. Further work is needed to better understand natural particle characteristics, size distributions, and aggregation mechanisms. However, if this is a common natural process within hydrothermal plumes, then it is important to consider how aggregation may influence particle transport. Though we cannot estimate a bulk settling rate from this data, we can use our spectromicroscopy observations and a few key assumptions (following German and Sparks, 1993), to illustrate the transport implications of aggregation on the material in our samples. We do so by using Stokes' equation to compare particle settling velocities for aggregated (typical observation) plume particles and their unaggregated (atypical observation) organic and inorganic constituents. In this approach, particles are idealized as axially symmetric spheres. For the organic phase, we assume a density of 1035 kg m^{-3} , which is equivalent to the

density of ambient seawater, and consistent with conceptual models of transparent exopolymer formation and transport (Alldredge and Crocker, 1995). For the inorganic phase, we assume an average density of 4450 kg m^{-3} , equivalent to a 50:50 mixture of pyrrhotite and Fe oxyhydroxide (i.e., goethite) for which the respective mineral densities are 4300 and 4600 kg m^{-3} (Downs and Hall-Wallace, 2003). Separate settling rate estimates were made for unaggregated organic and inorganic phases based on calculations for homogenous spheres of those materials (see Section 2.6). A settling rate estimate for an aggregate of inorganic and organic material was based on a $10 \mu\text{m}$ sphere comprised of an organic matrix embedded with 25 mineral grains of a $\sim 0.25 \mu\text{m}$ diameter. The effective density of an aggregate with these characteristics can be estimated from $\rho_a = D_a^{-3}[\rho_o D_a^3 - n\rho_o D_i^3 + n\rho_i D_i^3]$, where ρ_a , ρ_o , and ρ_i are the respective densities, and D_a , D_i , and D_o the respective diameters, of the entire aggregate and the constituent organic and inorganic phases, and n is the number of mineral grains. The effective density of this example aggregate is 1036 kg m^{-3} , and the Stokes' settling velocity is 0 for the neutrally buoyant organic matter, 0.0064 m d^{-1} for a $0.25 \mu\text{m}$ mineral grain, and 0.0030 m d^{-1} for the aggregate. Again these calculations do not represent bulk characteristics.

German and Sparks (1993) calculated bulk settling rates for material collected from the TAG Mid-Atlantic Ridge hydrothermal plume by sediment traps; they ranged between 4 and 8 m d^{-1} for coarse grained $10 \mu\text{m}$ diameter mineral grains and $0.2\text{--}0.3 \text{ m d}^{-1}$ for fine-grained $2 \mu\text{m}$ diameter mineral grains. Conversely the German and Sparks (1993) estimates do not apply to any material (e.g., slow settling or neutrally buoyant) that was not exported as a near field settling flux. The purpose of our calculation is not to reconcile these observations; we lack the data to do so. The purpose is simply to illustrate how aggregation can enhance the removal of organic material to the seafloor while enhancing the dispersal of hydrothermal elements to the water-column. In the latter case, the effect would be additive to enhanced dispersal of hydrothermal metals by complexation with organic matter as recently observed by Bennett et al. (2008). In the former case, the effect would deliver Fe aggregated organic C to the sediments in a form that could predispose that C to enhanced preservation during subsequent burial (Lalonde et al., 2012). The ubiquity of these inorganic interactions with dissolved and particulate organic matter is not known, but the role of organic matter in sedimentation and dispersal of hydrothermal elements cannot be neglected in future models of hydrothermal processes.

These results evoke several open hypotheses associated with hydrothermal plume particle formation that must be addressed in order to fully understand the biogeochemical effects of hydrothermal venting on the overlying water column. One key to addressing them will be the systematic collection of samples along the full plume transport path – starting in the buoyant rather than just the young nonbuoyant plume (cf. Kadko et al., 1990; Cave et al., 2002; Edmonds and German, 2004). Another important contribution would be a study of the long-term variability in

plume chemistry and mineralogy. But what has also become increasingly apparent from recent results (Shackelford and Cowen, 2006; Prieto and Cowen, 2007; Toner et al., 2009; this study), is that it will be essential to incorporate organic particulate processes into our future conceptual models of hydrothermal plume formation and transport.

4.4. Plume biogeochemistry of sulfur and carbon

At the EPR, S-rich biogenic material can be a significant, but episodic, component of near-bottom vent field waters and rising hydrothermal plumes (Haymon et al., 1993). In that case, the 1991 seafloor eruption led to the catastrophic venting and entrainment of large flocs (cm scale) of seafloor and subseafloor mats of H₂S-oxidizing *Arcobacter* (Taylor and Wirsen, 1997). Feely et al. (1994) observed high concentrations of S-rich particulate organic matter at nonbuoyant plume height when sampling ~ 9 months later and above the same site. More recently, Toner et al. (2009) observed that particulate organic matter was also common in post eruption (2006) sediment traps, and hypothesized that organo-S compounds were present. In agreement with these findings, we observe that S-rich flocs of organic material were prevalent at non-buoyant plume height, but these samples were collected 18–24 months following the most recent (winter 2005–06) eruption (Fig. 6).

We hypothesize that the S-rich organic material we have observed in plumes at the nonbuoyant plume height above the EPR is produced chronically in the plume by endemic deep-sea microbes. This would be in contrast with Feely et al. (1994) who hypothesized that the material they observed at nonbuoyant plume height was of the same origin as that reported by Haymon et al. (1993): *Arcobacter* detritus expulsed from the seafloor as a result of volcanic eruptions. It is proven that S-rich organic material is periodically expulsed from the seafloor; but this does not preclude chronic production in the water column. Our results, show this S-rich material is present in the water column >1.5 years post eruption. This does not preclude eruptive discharge, but it raises sufficient doubt for us to propose that production may also be chronic and possibly occurring in the plume. In support of our hypothesis, a ubiquitous deep-sea, SUP05-like *Gammaproteobacteria* (Walsh et al., 2009), known to be prevalent in hydrothermal plumes (Dick and Tebo, 2010), has recently been found capable of S-oxidation. Further, Sylvan et al. (2012) report a high percentage of S-oxidizing *Epsilonproteobacteria*, as well as *Gammaproteobacteria*, among the microbial communities in sediment trap samples collected from the same area as this study.

The composition of the plume particulate organic matter (polysaccharides, proteins) also suggests that vent derived chemosynthesis (sub-seafloor, seafloor, or plume) is affecting plume processes. This is consistent with recent observations by Bennett et al. (2011) of elevated particulate organic matter concentrations in hydrothermal plumes of the same area. It is also consistent with reports of hydrothermal plume organic material at other sites, including for example, the presence of dissolved organic matter at 5 S

Mid-Atlantic Ridge (Bennett et al., 2008), and lipid-rich ascending particle fluxes at the Endeavor Segment of the Juan de Fuca Ridge (Cowen et al., 2001; Wakeham et al., 2001). Accordingly, we hypothesize that these observations at EPR, Mid-Atlantic Ridge, and Juan de Fuca Ridge represent related processes typical of hydrothermal plumes. At this time, dissolved and particulate organic matter are not included in conceptual hydrothermal plume models. New models for plume processes will be required in the future, therefore, that accommodate a more biogeochemical approach to hydrothermal systems that addresses the origins and properties of organic matter, organic–inorganic aggregation processes, and mineral surface reactivity in the presence of organic coatings.

5. CONCLUSIONS

The nonbuoyant plume environment is characterized by temporal and spatial heterogeneity and chemical disequilibria. Major mineral forming elements like Fe, Mn, and S were observed in oxidized and reduced phases within the same sample, and often within the same particle aggregate. In addition, trace element incorporation by individual mineral particles is non-uniform despite positive linear correlations in the bulk. Particle aggregation with organic materials is prevalent in descending and nonbuoyant fluxes at this site. Based on current understanding of surface chemistry, both particle aggregation and surface coatings will influence the reactivity and fate of hydrothermal particulates. Flocculant, S-rich materials are present in the nonbuoyant plume even in the absence of seafloor eruptions. These observations are consistent with non-eruptive sources of S, including entrained materials from near vent biomass (seafloor chemosynthesis) and *in situ* production by S oxidizing microorganisms (water column chemosynthesis), and highlight the degree to which microbial activity may regulate hydrothermal fluxes. This study confirms that the organic/inorganic micro-aggregates and Fe(II) enriched organic material observed previously in sediment trap samples collected from this area are also present in the overlying water-column plume. Our results illustrate the remarkable geochemical complexity that can be produced by the hydrothermal plume particle formation process. This geochemical complexity, and the range of material properties it implies, has the potential to influence how far hydrothermal material is transported from its source and how hydrothermal plumes may modify the gross exchange of material between the lithosphere and seawater.

ACKNOWLEDGMENTS

We would like to thank Lauren Mullenax and the R/V Atlantis cruise AT15-26 (LADDER 2007) crew and science party (NSF OCE-0424953) for allowing us to conduct our sampling, and Steven Manganini and Olivier Rouxel for assistance with sample processing. The Woods Hole Oceanographic Institution's Deep Ocean Exploration Institute funded construction of the SUPR sampler. Postdoctoral support for JAB was through RIDGE 2000 (NSF OCE-0550331); Mike Purcell and John Fetterman (WHOI), and Ken Doherty, Michael Mathewson, Ivory Engstrom, and Tim Shanahan (McLane Research Laboratories Inc.) all made

significant contributions during the SUPR sampler development. Part of this work was carried out at the Institute of Technology, Characterization Facility, University of Minnesota (an NSF-funded Materials Research Facilities Network), in particular we thank Maria Torija for assistance with JADE. We thank T. Tyliszczak for support at ALS BL11.0.2, Amanda Turner and Katrina Edwards for ALS BL 10.3.2 beam time assistance, Dean Hesterberg for providing S reference spectra, Clara Chan for providing a ferrihydrite specimen and Shawn French (U. Guelph) for providing a lipid specimen. BMT acknowledges support from the Office of the Vice President for Research, University of Minnesota. The Advanced Light Source (SCF, MAM) is supported by the Office of Science, Basic Energy Sciences, Division of Materials Science of the U.S. Department of Energy (DE-AC02-05CH11231). CRG acknowledges support from NSF Grant OCE-0647948. AMT acknowledges support from NSF Grant OCE-0425361.

APPENDIX A. SUPPLEMENTARY DATA

Supplementary data associated with this article can be found, in the online version, at <http://dx.doi.org/10.1016/j.gca.2012.04.003>.

REFERENCES

- Alldredge A. L. and Crocker K. M. (1995) Why do sinking mucilage aggregates accumulate in the water column? *Sci. Total Environ.* **165**, 15–22.
- Alibo D. S. and Nozaki Y. (1999) Rare earth elements in seawater: particle association, shale-normalization, and Ce oxidation. *Geochim. Cosmochim. Acta* **63**, 363–372.
- Bennett S. A., Achterberg E. P., Connelly D. P., Statham P. J., Fones G. R. and German C. R. (2008) The distribution and stabilisation of dissolved Fe in deep-sea hydrothermal plumes. *Earth Planet. Sci. Lett.* **270**, 157–167.
- Bennett S. A., Statham P. J., Green D. R. H., Statham P. J., le Bris N., McDermott J., Prado F., Rouxel O. J., Von Damm K. L. and German C. R. (2011) Dissolved and particulate organic carbon in hydrothermal plumes from the East Pacific Rise, 9°50'N. *Deep Sea Res. Pt. I* **58**, 922–931.
- Bethke C. M. (2007) *Geochemical and Biogeochemical Reaction Modeling*. Cambridge University Press, Cambridge, UK.
- Boström K. and Peterson M. N. A. (1969) The origin of aluminum-poor ferromanganese sediments in areas of high heat flow on the East Pacific Rise. *Mar. Geol.* **7**, 427–447. [http://dx.doi.org/10.1016/0025-3227\(69\)90016-4](http://dx.doi.org/10.1016/0025-3227(69)90016-4).
- Bowers T. S., Von Damm K. L. and Edmond J. M. (1985) Chemical evolution of mid-ocean ridge hot springs. *Geochim. Cosmochim. Acta* **49**, 2239–2252.
- Boyce C. K., Cody G. D., Feser M., Jacobsen C., Knoll A. H. and Wirick S. (2002) Organic chemical differentiation within fossil plant cell walls detected with X-ray spectromicroscopy. *Geology* **30**, 1039–1042.
- Brandes J. A., Lee C., Wakeham S., Peterson M., Jacobsen C., Wirick S. and Cody G. (2004) Examining marine particulate organic matter at sub-micron scales using scanning transmission X-ray microscopy and carbon X-ray absorption near edge structure spectroscopy. *Mar. Chem.* **92**, 107–121.
- Breier J. A., Rauch C. G., McCartney K., Toner B. M., Faksa S. C., White S. N. and German C. R. (2009) A suspended-particle rosette multi-sampler for discrete biogeochemical sampling in low-particle-density waters. *Deep Sea Res. Pt. I* **56**, 1579–1589. <http://dx.doi.org/10.1016/J.DSR.2009.04.005>.

- Byrne R. H. and Sholkovitz E. R. (1996) Marine chemistry and geochemistry of the lanthanides. In *Handbook of the Physics and Chemistry of Rare Earth Elements*, 23, pp. 497–593. Handbook of the Physics and Chemistry of Rare Earth Elements. Elsevier, London.
- Carbotte S. and MacDonald K. (1992) East Pacific Rise 8°–10°30'N: evolution of ridge segments and discontinuities from SeaMARC II and three-dimensional magnetic studies. *J. Geophys. Res.* **97**, 6959–6982.
- Cave R. R., German C. R., Thomson J. and Nesbitt R. W. (2002) Fluxes to sediments underlying the Rainbow hydrothermal plume at 36°14'N on the Mid-Atlantic Ridge. *Geochim. Cosmochim. Acta* **66**, 1905–1923.
- Chan C. S., Fakra S. C., Edwards D. C., Emerson D. and Banfield J. F. (2009) Iron oxyhydroxide mineralization on microbial extracellular polysaccharides. *Geochim. Cosmochim. Acta* **73**, 3807–3818.
- Cleverley J. S. and Bastrakov E. N. (2005) K2GWB: utility for generating thermodynamic data files for The Geochemist's Workbench at 0–1000 °C and 1–5000 bar from UT2K and the UNITHERM database. *Comput. Geosci.* **31**, 756–767.
- Cody G. D., Ade H., Wirick S., Mitchell G. D. and Davis A. (1998) Determination of chemical-structural changes in vitrinite accompanying luminescence alteration using C-NEXAFS analysis. *Org. Geochem.* **28**, 441–455.
- Cody G. D., Heying E., Alexander C. M. O., Nittler L. R., Kilcoyne A. L. D., Sandford S. A. and Stroud R. M. (2011) Establishing a molecular relationship between chondritic and cometary organic acids. *Proceedings of the National Academy of Sciences of the United States of America, early on-line edition*. <http://dx.doi.org/10.1073/pnas.1015913108>.
- Cowen J. P., Massoth G. J. and Baker E. T. (1986) Bacterial scavenging of Mn and Fe in a mid-field to far-field hydrothermal particle plume. *Nature* **322**, 169–171.
- Cowen J. P., Bertram M. A., Wakeham S. G., Thomson R. E., Lavelle J. W., Baker E. T. and Feely R. A. (2001) Ascending and descending particle flux from hydrothermal plumes at Endeavour Segment, Juan de Fuca Ridge. *Deep Sea Res. Pt. I* **48**, 1093–1120.
- De Angelis M. A., Lilley M. D. and Baross J. A. (1993) Methane oxidation in deep-sea hydrothermal plumes of the Endeavour Segment of the Juan de Fuca Ridge. *Deep Sea Res. Pt. I* **40**, 1169–1186.
- Dick G. J., Clement B. G., Webb S. M., Fodrie F. J., Bargar J. R. and Tebo B. M. (2009) Enzymatic microbial Mn(II) oxidation and Mn biooxide production in the Guaymas Basin deep-sea hydrothermal plume. *Geochim. Cosmochim. Acta* **73**, 6517–6530.
- Dick G. J. and Tebo B. M. (2010) Microbial diversity and biogeochemistry of the Guaymas Basin deep-sea hydrothermal plume. *Environ. Microbiol.* **12**, 1334–1347.
- Downs R. T. and Hall-Wallace M. (2003) The American Mineralogist crystal structure database. *Am. Mineral.* **88**, 247–250.
- Drummond S. E. (1981) Boiling and mixing of hydrothermal fluids: chemical effects on mineral precipitation. Ph. D. thesis, Pennsylvania State University.
- Dymond J. and Roth S. (1988) Plume dispersed hydrothermal particles: a time-series record of settling flux from the Endeavour Ridge using moored sensors. *Geochim. Cosmochim. Acta* **52**, 2525–2536.
- Edmonds H. N. and German C. R. (2004) Particle geochemistry in the Rainbow hydrothermal plume, Mid-Atlantic Ridge. *Geochim. Cosmochim. Acta* **68**, 759–772.
- Elderfield H. and Schultz A. (1996) Mid-ocean ridge hydrothermal fluxes and the chemical composition of the ocean. *Annu. Rev. Earth Planet. Sci.* **24**, 191–224.
- Feely R. A., Massoth G. J., Baker E. T., Cowen J. P., Lamb M. F. and Krogslund K. A. (1990) The effect of hydrothermal processes on midwater phosphorus distributions in the northeast Pacific. *Earth Planet. Sci. Lett.* **96**, 305–318.
- Feely R. A., Trefry J. H., Massoth G. J. and Metz S. (1991) A comparison of the scavenging of phosphorus and arsenic from seawater by hydrothermal iron oxyhydroxides in the Atlantic and Pacific Oceans. *Deep Sea Res.* **38**, 617–623.
- Feely R. A., Massoth G. J., Baker E. T., Lebon G. T. and Geiselman T. L. (1992) Tracking the dispersal of hydrothermal plumes from the Juan de Fuca Ridge using suspended matter compositions. *J. Geophys. Res.* **97**, 3457–3468.
- Feely R. A., Gendron J. F., Baker E. T. and Lebon G. T. (1994) Hydrothermal plumes along the East Pacific Rise, 8°40' to 11°50'N – particle distribution and composition. *Earth Planet. Sci. Lett.* **128**, 19–36.
- Feely R. A., Trefry J. H., Lebon G. T. and German C. R. (1998) The relationship between P/Fe and V/Fe ratios in hydrothermal precipitates and dissolved phosphate in seawater. *Geophys. Res. Lett.* **25**, 2253–2256.
- Ferrini V. L., Fornari D. J., Shank T. M., Kinsey J. C., Tivey M. A., Soule S. A., Carbotte S. M., Whitcomb L. L., Yoerger D. and Howland J. (2007) Submeter bathymetric mapping of volcanic and hydrothermal features on the East Pacific Rise crest at 9 degrees 50'N. *Geochim. Geophys. Geosyst.* **8**, Q01006. <http://dx.doi.org/10.1029/2006GC001333>.
- Field M. P. and Sherrell R. M. (2000) Dissolved and particulate Fe in a hydrothermal plume at 9°45'N, East Pacific Rise: slow Fe(II). *Geochim. Cosmochim. Acta* **64**, 619–628.
- Fornari D. J., Shank T., Von Damm K. L., Gregg T. K. P., Lilley M., Levai G., Bray A., Haymon R. M., Perfit M. R. and Lutz R. (1998) Time-series temperature measurements at high-temperature hydrothermal vents, East Pacific Rise 9 degrees 49'–51'N: evidence for monitoring a crustal cracking event. *Earth Planet. Sci. Lett.* **160**, 419–431.
- German C. R. and Sparks R. S. J. (1993) Particle recycling in the TAG hydrothermal plume. *Earth Planet. Sci. Lett.* **116**, 129–134.
- German C. R., Klinkhammer G. P., Edmond J. M., Mitra A. and Elderfield H. (1990) Hydrothermal scavenging of rare-earth elements in the ocean. *Nature* **345**, 516–518.
- German C. R., Fleer A. P., Bacon M. P. and Edmond J. M. (1991a) Hydrothermal scavenging at the Mid-Atlantic Ridge: radionuclide distributions. *Earth Planet. Sci. Lett.* **105**, 170–181.
- German C. R., Campbell A. C. and Edmond J. M. (1991b) Hydrothermal scavenging at the Mid-Atlantic Ridge: modification of trace element dissolved fluxes. *Earth Planet. Sci. Lett.* **107**, 101–114.
- German C. R., Bourles D. L., Brown E. T., Hergt J., Colley S., Higgs N. C., Ludford E. M., Nelsen T. A., Feely R. A., Raisbeck G. and Yiou F. (1997) Hydrothermal scavenging on the Juan de Fuca Ridge: $^{230}\text{Th}_{\text{xs}}$, ^{10}Be , and REEs in ridge-flank sediments. *Geochim. Cosmochim. Acta* **61**, 4067–4078.
- German C. R., Colley S., Palmer M. R., Khripounoff A. and Klinkhammer G. P. (2002) Hydrothermal plume-particle fluxes at 13 degrees N on the East Pacific Rise. *Deep Sea Res. Pt. I* **49**, 1921–1940.
- Govindaraju K. (1994) 1994 Compilation of working values and sample description for 383 geostandards. *Geostand. Geoanal. Res.* **18**, 1639–4488.
- Hammersley A. P., Svensson S. O., Hanfland M., Fitch A. N. and Hausermann D. (1996) Two-dimensional detector software: from real detector to idealized image or two-theta scan. *High. Press. Res.* **14**, 235–248.
- Haymon R. M., Fornari D. J., Von Damm K. L., Lilley M. D., Perfit M. R., Edmond J. M., Shanks W. C., Lutz R. A.,

- Grebmeier M., Carbotte S., Wright D., McLaughlin E., Smith M., Beedle N. and Olson E. (1993) Volcanic-eruption of the midocean ridge along the East Pacific Rise crest at 9°45'–52'N – direct submersible observations of sea-floor phenomena associated with an eruption event in April, 1991. *Earth Planet. Sci. Lett.* **119**, 85–101.
- Helgeson H. C. (1969) Thermodynamics of hydrothermal systems at elevated temperatures and pressures. *Am. J. Sci.* **267**, 729–804.
- Helgeson H. C. and Kirkham D. H. (1974) Theoretical prediction of the thermodynamic behavior of aqueous electrolytes at high pressures and temperatures; II, Debye-Hückel parameters for activity coefficients and relative partial molal properties. *Am. J. Sci.* **274**, 1199–1261.
- Helgeson H. C., Delaney J. M., Nesbitt H. W. and Bird D. K. (1978) Summary and critique of the thermodynamic properties of rock-forming minerals. *Am. J. Sci.* **278-A**, 1–229.
- Janecky D. R. and Seyfried W. E. (1984) Formation of massive sulfide deposits on oceanic ridge crests – incremental reaction models for mixing between hydrothermal solutions and seawater. *Geochim. Cosmochim. Acta* **48**, 2723–2738.
- Johnson J. W., Oelkers E. H. and Helgeson H. C. (1992) SUPCRT92: a software package for calculating the standard molal thermodynamic properties of minerals, gases, aqueous species, and reactions from 1 to 5000 bar and 0 to 1000 °C. *Comput. Geosci.* **18**, 899–947.
- Kadko D. (1993) An assessment of the effect of chemical scavenging within submarine hydrothermal plumes upon ocean geochemistry. *Earth Planet. Sci. Lett.* **120**, 361–374.
- Kadko D. C., Rosenberg N. D., Lupton J. E., Collier R. W. and Lilley M. D. (1990) Chemical reaction rates and entrainment within the Endeavour Ridge hydrothermal plume. *Earth Planet. Sci. Lett.* **99**, 315–335.
- Kadko D., Feely R. and Massoth G. (1994) Scavenging of Th-234 and phosphorus removal from the hydrothermal effluent plume over the North Cleft segment of the Juan de Fuca Ridge. *J. Geophys. Res. Solid Ea* **99**, 5017–5024.
- Kadko D., Baross J. and Alt J. (1995) Hydrothermal fluxes and global change. In *Seafloor Hydrothermal Systems: Physical, Chemical, Biological and Geological Interactions*, 91 (eds. S. E. Humphris, L. Mullineaux, R. Zierenberg and R. Thomson). AGU, Washington, DC, pp. 446–466.
- Khrisponoff A. and Alberic P. (1991) Settling of particles in a hydrothermal vent field (East Pacific Rise 13° N) measured with sediment traps. *Deep Sea Res. Pt. I* **38**, 729–744.
- Khrisponoff A., Vangriesheim A., Crassous P., Segonzac M., Lafon V. and Warén A. (2008) Temporal variation of currents, particulate flux and organism supply at two deep-sea hydrothermal fields of the Azores Triple Junction. *Deep Sea Res. Pt. I* **55**, 532–551.
- Kilcoyne A. L. D., Tyliszczak T., Steele W. F., Fakra S., Hitchcock P., Franck K., Anderson E., Harteneck B., Rightor E. G., Mitchell G. E., Hitchcock A. P., Yang L., Warwick T. and Ade H. (2003) Interferometer-controlled scanning transmission X-ray microscopes at the Advanced Light Source. *J. Synchrotron Rad.* **10**, 125–136.
- Klinkhammer G. P., Elderfield H. and Hudson A. (1983) Rare earth elements in seawater near hydrothermal vents. *Nature* **305**, 185–188. <http://dx.doi.org/10.1038/305185a0>.
- Klinkhammer G., German C. R., Elderfield H., Greaves M. J. and Mitra A. (1994) Rare-earth elements in hydrothermal fluids and plume particulates by inductively-coupled plasma-mass spectrometry. *Mar. Chem.* **45**, 179–186.
- Kraft S., Stümpel J. and Kuettgens U. (1996) High resolution X-ray absorption spectroscopy with absolute energy calibration for the determination of absorption edge energies. *Rev. Sci. Instrum.* **67**, 681–687.
- Lalonde K., Mucci A., Ouellet A. and Gélinas Y. (2012) Preservation of organic matter in sediments promoted by iron. *Nature* **483**, 198–200.
- Lam P., Cowen J. P., Popp B. N. and Jones R. D. (2008) Microbial ammonia oxidation and enhanced nitrogen cycling in the Endeavour hydrothermal plume. *Geochim. Cosmochim. Acta* **72**, 2268–2286.
- Lupton J. E., Delaney J. R., Johnson H. P. and Tivey M. K. (1985) Entrainment and vertical transport of deep-ocean water by buoyant hydrothermal plumes. *Nature* **316**, 621–623.
- Malinowski E. R. (1977) Determination of the number of factors and the experimental error in a data matrix. *Anal. Chem.* **49**, 612–617.
- Malinowski E. R. (1978) Theory of error for target factor analysis with applications to mass spectrometry and nuclear magnetic resonance spectrometry. *Anal. Chim. Acta* **103**, 339–354.
- Manceau A., Marcus M. A. and Tamura N. (2002) Quantitative speciation of heavy metals in soils and sediments by synchrotron X-ray techniques. In *Applications of Synchrotron Radiation in Low-Temperature Geochemistry and Environmental Science* (eds. P. A. Fenter, M. L. Rivers, N. C. Sturchio and S. R. Sutton). Mineralogical Society of America, Washington, DC.
- Mandernack K. W. and Tebo B. M. (1993) Manganese scavenging and oxidation at hydrothermal vents and in vent plumes. *Geochim. Cosmochim. Acta* **57**, 3907–3923.
- Marcus M. A., MacDowell A., Celestre R., Manceau A., Miller T., Padmore H. A. and Sublett R. E. (2004) Beamline 10.3.2 at ALS: a hard X-ray microprobe for environmental and material sciences. *J. Synchrotron Rad.* **11**, 239–247.
- Marcus M. A., Westphal A. J. and Fakra S. (2008) Classification of Fe-bearing species from K-edge XANES data using two-parameter correlation plots. *J. Synchrotron Rad.* **15**, 463–468.
- McCollom T. M. (2000) Geochemical constraints on primary productivity in submarine hydrothermal vent plumes. *Deep Sea Res. Pt. I* **47**, 85–101.
- McCollom T. M. and Shock E. L. (1997) Geochemical constraints on chemolithoautotrophic metabolism by microorganisms in seafloor hydrothermal systems. *Geochim. Cosmochim. Acta* **61**, 4375–4391.
- Mottl M. J. and McConachy T. F. (1990) Chemical processes in buoyant hydrothermal plumes on the East Pacific Rise near 21° N. *Geochim. Cosmochim. Acta* **54**, 1911–1927.
- Mynevi S. C. B. (2002) Soft X-ray spectroscopy and spectromicroscopy studies of organic molecules in the environment. *Applications of Synchrotron Radiation in Low-Temperature Geochemistry and Environmental Sciences* **49**, 485–579.
- O'Brien D., Carton M. D., Eardly D. and Patching J. W. (1998) *In situ* filtration and preliminary molecular analysis of microbial biomass from the Rainbow hydrothermal plume at 36°15'N on the Mid-Atlantic Ridge. *Earth Planet. Sci. Lett.* **157**, 223–231.
- Olivarez A. M. and Owen R. M. (1989) REE/Fe variations in hydrothermal sediments: implications for the REE content of seawater. *Geochim. Cosmochim. Acta* **53**, 757–762.
- Owen R. M. and Olivarez A. M. (1988) Geochemistry of rare earth elements in pacific hydrothermal sediments. *Mar. Chem.* **25**, 183–196.
- Prieto L. and Cowen J. (2007) Transparent exopolymer particles in a deep-sea hydrothermal system: Guaymas Basin, Gulf of California. *Mar. Biol.* **150**, 1093–1101.
- Proskurowski G., Lilley M. D. and Olson E. J. (2008) Stable isotopic evidence in support of active microbial methane cycling in low-temperature diffuse flow vents at 9°50'N East Pacific Rise. *Geochim. Cosmochim. Acta* **72**, 2005–2023.

- Robie R. A., Hemingway B. S. and Fisher J. R. (1979) *Thermodynamic properties of minerals and related substances at 298.15 K and 1 bar (10 pascals) pressure and at higher temperatures*. U.S. Geological Survey bulletin 1452, U.S. Geological Survey, Reston, VA.
- Rudnicki M. D. and Elderfield H. (1993) A chemical-model of the buoyant and neutrally buoyant plume above the Tag Vent field, 26 degrees-N, Mid-Atlantic Ridge. *Geochim. Cosmochim. Acta* **57**, 2939–2957.
- Ruhlin D. E. and Owen R. M. (1986) The rare earth element geochemistry of hydrothermal sediments from the East Pacific Rise: examination of a seawater scavenging mechanism. *Geochim. Cosmochim. Acta* **50**, 393–400.
- Saccoccia P. J. and Seyfried, Jr., W. E. (1994) The solubility of chlorite solid solutions in 3.2 wt% NaCl fluids from 300–400 °C, 500 bars. *Geochim. Cosmochim. Acta* **58**, 567–585.
- Sander S. G. and Koschinsky A. (2011) Metal flux from hydrothermal vents increased by organic complexation. *Nat. Geosci.* **4**, 145–150.
- Sander S. G., Koschinsky A., Massoth G., Stott M. and Hunter K. A. (2007) Organic complexation of copper in deep-sea hydrothermal vent systems. *Environ. Chem.* **4**, 81–89.
- Sandford S. A., Alón J., Alexander C. M. O. D., Araki T., Bajt S., Baratta G. A., Borg J., Bradley J. P., Brownlee D. E., Brucato J. R., Burchell M. J., Busemann H., Butterworth A., Clemett S. J., Cody G., Colangeli L., Cooper G., D'Hendecourt L., Djouadi Z., Dworkin J. P., Ferrini G., Fleckenstein H., Flynn G. J., Franchi I. A., Fries M., Gilles M. K., Glavin D. P., Gounelle M., Grossemey F., Jacobsen C., Keller L. P., Kilcoyne A. L. D., Leitner J., Matrajt G., Meibom A., Mennella V., Mostefaoui S., Nittler L. R., Palumbo M. E., Papanastassiou D. A., Robert F., Rotundi A., Snead C. J., Spencer M. K., Stadermann F. J., Steele A., Stephan T., Tsou P., Tyliszczak T., Westphal A. J., Wirick S., Wopenka B., Yabuta H., Zare R. N. and Zolensky M. E. (2006) Organics captured from comet 81P/Wild 2 by the stardust spacecraft. *Science* **314**, 1720–1724.
- Sands C. M., Connelly D. P., Statham P. J. and German C. R. (2012) Size fractionation of trace metals in the Edmond hydrothermal plume, Central Indian Ocean. *Earth Planet. Sci. Lett.* **319–320**, 15–22. <http://dx.doi.org/10.1016/j.epsl.2011.12.031>.
- Shackelford R. and Cowen J. P. (2006) Transparent exopolymer particles (TEP) as a component of hydrothermal plume particle dynamics. *Deep Sea Res. Pt. I* **53**, 1677–1694.
- Shank T. M., Fornari D. J., Von Damm K. L., Lilley M. D., Haymon R. M. and Lutz R. A. (1998) Temporal and spatial patterns of biological community development at nascent deep-sea hydrothermal vents (9° 50'N, East Pacific Rise). *Deep Sea Res. Pt. II* **45**, 465–515.
- Sherrell R. M., Field M. P. and Ravizza G. (1999) Uptake and fractionation of rare earth elements on hydrothermal plume particles at 9°45'N, East Pacific Rise. *Geochim. Cosmochim. Acta* **63**, 1709–1722.
- Shock E. L. and Helgeson H. C. (1988) Calculation of the thermodynamic and transport properties of aqueous species at high pressures and temperatures: correlation algorithms for ionic species and equation of state predictions to 5 kb and 1000 °C. *Geochim. Cosmochim. Acta* **52**, 2009–2036.
- Shock E. L., Helgeson H. C. and Sverjensky D. A. (1989) Calculation of the thermodynamic and transport properties of aqueous species at high pressures and temperatures: standard partial molal properties of inorganic neutral species. *Geochim. Cosmochim. Acta* **53**, 2157–2183.
- Shock E. L., Sassani D. C., Willis M. and Sverjensky D. A. (1997) Inorganic species in geologic fluids: correlations among standard molal thermodynamic properties of aqueous ions and hydroxide complexes. *Geochim. Cosmochim. Acta* **61**, 907–950.
- Solomon D., Lehmann J., Kinyangi J., Liang B. Q., Heymann K., Dathe L., Hanley K., Wirick S. and Jacobsen C. (2009) Carbon (1s) NEXAFS spectroscopy of biogeochemically relevant reference organic compounds. *Soil Sci. Soc. Am. J.* **73**, 1817–1830.
- Soule S. A., Fornari D. J., Perfit M. R. and Rubin K. H. (2007) New insights into mid-ocean ridge volcanic processes from the 2005–2006 eruption of the East Pacific Rise, 9°46'N–9°56'N. *Geology* **35**, 1079–1082.
- Stöhr J. (1992) *NEXAFS Spectroscopy*. Springer-Verlag, Berlin.
- Sverjensky D. A., Shock E. L. and Helgeson H. C. (1997) Prediction of the thermodynamic properties of aqueous metal complexes to 1000 °C and 5 kb. *Geochim. Cosmochim. Acta* **61**, 1359–1412.
- Sylvan J. B., Pyenson B. C., Rouxel O., German C. R. and Edwards K. J. (Ivan et al., xxxx) Time-series analysis of two hydrothermal plumes at 9° 50'N East Pacific Rise reveals distinct, heterogeneous bacterial populations. *Geobiology* **10**, 178–192.
- Tagliabue A., Bopp L., Dutay J.-C., Bowie A. R., Chever F., Jean-Baptiste P., Bucciarelli E., Lannuzel D., Remenyi T., Sarthou G., Aumont O., Gehlen M. and Jeandel C. (2010) Hydrothermal contribution to the oceanic dissolved iron inventory. *Nat. Geosci.* **3**, 252–256. <http://dx.doi.org/10.1038/ngeo1818>.
- Talley L. D. (2007) Hydrographic Atlas of the World Ocean Circulation Experiment (WOCE). In *Pacific Ocean*, vol. 2 (eds. M. Sparrow, P. Chapman and J. Gould). International WOCE Project Office, Southampton, UK.
- Taylor S. R. and McLennan S. M. (1985) *The Continental Crust: Its Composition and Evolution*. Blackwell, Boston.
- Taylor C. D. and Wirsen C. O. (1997) Microbiology and ecology of filamentous sulfur formation. *Science* **277**, 1483–1485.
- Thurnherr A. M., Ledwell J. R., Lavelle J. W. and Mullineaux L. S. (2011) Hydrography and circulation near the crest of the East Pacific Rise between 9° and 10°N. *Deep Sea Res. Pt. I* **58**, 365–376.
- Tolstoy M., Cowen J. P., Baker E. T., Fornari D. J., Rubin K. H., Shank T. M., Waldhauser F., Bohnenstiel D. R., Forsyth D. W., Holmes R. C., Love B., Perfit M. R., Weekly R. T., Soule S. A. and Glazer B. (2006) A sea-floor spreading event captured by seismometers. *Science* **314**, 1920–1922.
- Toner B., Manceau A., Webb S. M. and Sposito G. (2006) Zinc sorption to biogenic hexagonal-birnessite particles within a hydrated bacterial biofilm. *Geochim. Cosmochim. Acta* **70**, 27–43.
- Toner B. M., Fakra S. C., Manganini S. J., Santelli C. M., Marcus M. A., Moffett J., Rouxel O., German C. R. and Edwards K. J. (2009) Preservation of iron(II) by carbon-rich matrices in a hydrothermal plume. *Nat. Geosci.* **2**, 197–201. <http://dx.doi.org/10.1038/ngeo433>.
- Toner B. M., Marcus M. A., Edwards K. J., Rouxel O. and German C. R. (2012) Measuring the form of iron in hydrothermal plume particles. *Oceanography* **25**, 209–212.
- Trocine R. P. and Trefry J. H. (1988) Distribution and chemistry of suspended particles from an active hydrothermal vent site on the Mid-Atlantic Ridge at 26° N. *Earth Planet. Sci. Lett.* **88**, 1–15.
- Von Damm K. L. (2000) Chemistry of hydrothermal vent fluids from 9–10° N, East Pacific Rise: “time zero” the immediate posteruptive period. *J. Geophys. Res.* **105**, 11203–11222.
- Von Damm K. L. (2004) Evolution of the hydrothermal system at East Pacific Rise 9°50': geochemical evidence for changes in the upper oceanic crust. In *Mid-Ocean Ridges: hydrothermal interactions between the lithosphere and the oceans*, 148 (eds. C. R. German, J. Lin and L. M. Parson), pp. 285–304. Mid-Ocean Ridges: hydrothermal interactions between the lithosphere and the oceans. AGU, Washington, DC.

- Von Damm K. L., Edmond J. M., Grant B., Measures C. I., Walden B. and Weiss R. F. (1985) Chemistry of submarine hydrothermal solutions at 21°N, East Pacific Rise. *Geochim. Cosmochim. Acta* **49**, 2197–2220.
- Wagman D. D., Evans W. H., Parker V. B., Schumm R. H., Halow I., Bailey S. M., Churney K. L. and Nuttall R. L. (1982) *The NBS tables of chemical thermodynamic properties: selected values for inorganic and C1 and C2 organic substances in SI units*. American Chemical Society and the American Institute of Physics for the National Bureau of Standards, Washington, DC.
- Wakeham S. G., Cowen J. P., Burd B. J. and Thomson R. E. (2001) Lipid-rich ascending particles from the hydrothermal plume at Endeavour Segment, Juan de Fuca Ridge. *Geochim. Cosmochim. Acta* **65**, 923–939.
- Walsh D. A., Zaikova E., Howes C. G., Song Y. C., Wright J. J., Tringe S. G., Tortell P. D. and Hallam S. J. (2009) Metagenome of a versatile chemolithoautotroph from expanding oceanic dead zones. *Science* **326**, 578–582.
- Webb S. M. (2005) SIXPACK: a graphical user interface for XAS analysis using IFEFFIT. *Phys. Scr.* **T115**, 1011–1014.
- White S. M., Haymon R. M. and Carbotte S. M. (2006) A new view of ridge segmentation and near-axis volcanism at the East Pacific Rise, 8–12° N, from EM300 Multibeam Bathymetry (Data Brief). *Geochem. Geophys. Geosyst.* **7**. <http://dx.doi.org/10.1029/2006GC001407>.
- Winn C. D., Karl D. M. and Massoth G. J. (1986) Microorganisms in deep-sea hydrothermal plumes. *Nature* **320**, 744–746.
- Yucel M., Gartman A., Chan C. S. and Luther G. W. (2011) Hydrothermal vents as a kinetically stable source of iron-sulphide-bearing nanoparticles to the ocean. *Nat. Geosci.* **4**, 367–371.

Associate editor: Tom McCollom